

## ABSTRACT

Collisional depolarization of the atomic Cs  $6s^2S_{1/2} \rightarrow 10s^2S_{1/2}, 9d^2D_{5/2}$  transition with argon buffer gas

by Seda Kin

We report an experimental investigation of collisional depolarization of the atomic cesium  $6s^2S_{1/2} \rightarrow 10s^2S_{1/2}, 9d^2D_{5/2}$  two-color two-photon polarization spectrum. The Ar pressure dependence of the spectrum revealed strong depolarization in the vicinity of the  $6s^2S_{1/2} \rightarrow 6p^2P_{3/2} \rightarrow 10s^2S_{1/2}, 9d^2D_{5/2}$  stepwise resonances using short pulse pump-probe technique. The linear polarization degree was measured with the first laser tuned to resonance and the second laser tuned within  $\pm 11 \text{ cm}^{-1}$ . In the absence of collisions, the measured polarization spectrum is in excellent agreement with calculations. The collisional depolarization cross section which was deduced from the data is also in good agreement with the theory.

Collisional depolarization of the atomic Cs  $6s^2S_{1/2} \rightarrow 10s^2S_{1/2}, 9d^2D_{5/2}$  transition  
with argon buffer gas

A Thesis

Submitted to the

Faculty of Miami University

in partial fulfillment of

the requirements for the degree of

Master of Science

Department of Physics

by

Seda Kin

Miami University

Oxford, Ohio

2005

Advisor \_\_\_\_\_  
Burçin S. Bayram

Reader \_\_\_\_\_  
Douglas Marcum

Reader \_\_\_\_\_  
Samir Bali

# Contents

<b>1</b>	<b>Introduction</b>	<b>1</b>
<b>2</b>	<b>Theoretical Background</b>	<b>3</b>
2.1	Hamiltonian of the System . . . . .	3
2.2	Selection Rules . . . . .	6
2.3	Fine and Hyperfine Interactions . . . . .	8
2.4	Orientation and Alignment . . . . .	11
2.5	Linear Polarization Spectra . . . . .	12
2.6	Hyperfine Depolarization Effects on Polarization Spectra . . . . .	14
<b>3</b>	<b>Experimental Apparatus</b>	<b>16</b>
3.1	Lasers . . . . .	16
3.2	Polarization of the Light . . . . .	21
3.3	Oven and Cell . . . . .	22
3.4	Detection of the Signal and Data Processing . . . . .	25
<b>4</b>	<b>Overview of the Experiment</b>	<b>27</b>
<b>5</b>	<b>Results</b>	<b>29</b>
5.1	Data and Analysis . . . . .	29
5.2	Overview of the Measurements . . . . .	29
5.3	Linear Polarization Measurements . . . . .	30
5.4	Systematic Effects . . . . .	32
5.4.1	Temperature Effect . . . . .	34
5.4.2	Laser Power Effect . . . . .	35
5.4.3	Depolarization with Argon Buffer Gas . . . . .	36
5.4.4	Extracting the Depolarization Cross Section . . . . .	37
5.5	Conclusion . . . . .	43
<b>A</b>	<b>Density Matrix Elements</b>	<b>46</b>
<b>B</b>	<b>LabVIEW Program</b>	<b>52</b>
<b>C</b>	<b>Experimental Apparatus</b>	<b>56</b>

# List of Tables

5.1	Specifications of the lasers we used in the experiment. . . . .	31
5.2	Calculated and measured polarization degrees. . . . .	32
5.3	Our work on the depolarization with argon buffer gas in the $6s^2S_{1/2} \rightarrow 10s^2S_{1/2}$ transition. . . . .	39
5.4	Depolarization with argon buffer gas in the $6s^2S_{1/2} \rightarrow 9d^2D_{5/2}$ transition. . . . .	39
5.5	Constants used in Eq.5.16 to extract collisional depolarization cross section from the polarization spectrum (* [1]). . . . .	41
5.6	Collisionaldepolarization cross sections of the $6p^2P_{3/2}$ Cs atom . . . .	42
A.1	$(j_1 \frac{1}{2} m_1 m_2   j_1 \frac{1}{2} j m)$ . . . . .	48
A.2	$(j_1 \frac{3}{2} m_1 m_2   j_1 \frac{3}{2} j m)$ . . . . .	50
A.3	Clebsch-Gordan coefficients used in the experiment . . . . .	51

# List of Figures

2.1	Kastler diagram shows the selection rules and relative population on the selected atomic levels for $I_{\parallel}$ and $I_{\perp}$ . . . . .	6
2.2	Hyperfine splittings of the levels under study. . . . .	10
2.3	Geometry of the collision and detection frame. . . . .	11
2.4	Grotrian diagram shows us the excitation and emission scheme in cesium. . . . .	13
3.1	Schematic overview of experimental apparatus. . . . .	17
3.2	Pumping scheme of the experiment. . . . .	18
3.3	Littman-Metcalf cavity with grazing incidence design. . . . .	20
3.4	Micrometer tuning curve. . . . .	20
3.5	Geometry of the Experiment. . . . .	21
3.6	Cesium Ccell. . . . .	23
3.7	Oven with Cs cell inside. . . . .	23
3.8	View of the side and end windows of the oven. . . . .	24
3.9	Vapor pressure curve of Cs. . . . .	24
5.1	Energy level diagram for selected excited electronic states in atomic Cs. The figure also shows the approximate air wavelengths of the two-pulse laser light sources. The cascade fluorescence from the $9p^2P_{1/2}$ to $6s^2S_{1/2}$ is detected. . . . .	30
5.2	Polarization spectrum of the $6s^2S_{1/2} \rightarrow 10s^2S_{1/2}$ transition. . . . .	32
5.3	Polarization spectrum of the $6s^2S_{1/2} \rightarrow 9d^2D_{5/2}$ transition. . . . .	33
5.4	Polarization degree at various temperatures of Cs for the 6S-10S state excitation. . . . .	34
5.5	Polarization degree at various temperatures of Cs for the 6S-9D state excitation. . . . .	35
5.6	Power dependence of laser 1 on the polarization spectrum for the $9d^2D_{5/2}$ state. . . . .	36
5.7	Power dependence of laser 2 on the polarization spectrum for the $9d^2D_{5/2}$ state. . . . .	37
5.8	Depolarization of the $6s^2S_{1/2} \rightarrow 10s^2S_{1/2}, 9d^2D_{5/2}$ transition in the presence of different argon buffer gas pressures. . . . .	38
5.9	Weighted non-linear least square fit of the polarization spectrum of Cs in the vicinity of Ar atoms. . . . .	42
A.1	Kastler diagram of the levels for $I_{\parallel}$ . . . . .	47

A.2	Kastler diagram of the levels for $I_{\perp}$ .	49
B.1	Front panel of the LabVIEW control program.	52
B.2	Block diagram to control the stepper motor.	53
B.3	Stepper motor subVI.	53
B.4	Interface of the LCR.	54
B.5	Block diagram of the applied voltage on the LCR for perpendicular polarization.	54
B.6	Block diagram of the applied voltage on the LCR for parallel polarization.	55
B.7	Medowlark LCR subVI.	55
C.1	Experimental Apparatus.	56
C.2	Flowing dye laser 1 oscillator in the Littman-Metcalf design.	57
C.3	Dye flowing machine for laser 1.	57
C.4	Static dye laser 2 oscillator in the Littman-Metcalf design.	58
C.5	Dye laser 2 amplifier.	58
C.6	A view of the LCR and Glan-Thompson polarizer.	59
C.7	Boxcar averager/integrator.	59
C.8	DAQ board connected between a computer and the boxcar averager/integrator.	60

## ACKNOWLEDGMENTS

I would like to give my sincere thanks to my adviser Dr. Burçin Bayram for her patience, support, encouragement and guidance throughout my research. Her knowledge and experience in atomic physics helped me to complete my research and taught me extensive laboratory skills. I would like to also thank to my dissertation committee members Dr. Douglas Marcum and Dr. Samir Bali for their reading of this dissertation and helpful comments. Also, I would like to express my appreciation to Dr. Marcum, for his support and guidance during my advisers maternity leave. I would like to thank Professor Gönül Başar at Istanbul University who first introduced me to Atomic Molecular and Optical physics and supported me to come to the U.S.A. I would like to thank my friends and undergraduate assistants Morgan Welsh and Jacob Hinkle who contributed a lot of work for this investigation. Most importantly, I would like to thank my parents Halil and Gülten, my sister Cemre who emotionally supported and encouraged me during my study at Miami University in Oxford, OH. Finally, I would like to wish a great future and a lifetime happiness to the Bayram family with their newborn triplets Artun, Koray and Melisa Tuğçe.

# Chapter 1

## Introduction

The experimental study of the interaction of photons with matter is widely used in the field of atomic molecular and optical physics to understand the properties and behavior of the atoms and molecules. In present experiments with the developments of laser technology, laser light sources have been used to study photoionization or photodissociation, stimulated raman spectroscopy, polarization spectroscopy, laser cooling and trapping and recently in electromagnetically induced transparency (EIT) ([2], [3]). The use of lasers (coherent light sources) in spectroscopy is due to their high intensities in small frequencies and their good focusing properties. With the advent of tunable dye lasers, new types of investigations have become possible [4]. Dye lasers have been used in the single-photon, two-photon resonance and multi-photon excitation process to investigate the lifetimes of the atomic states or measuring the decay rates and atomic ionization due to their tunability properties. Two-photon excitation process have been mainly used to resolve the hyperfine structure [5] of the atoms and study quantum beat spectroscopy in the resolved hyperfine levels. Also, pulsed lasers become important in the time frame to investigate the alignment and orientation properties of the atom by using linearly or circularly polarized light sources. Alkali elements have been of great interest in laser spectroscopy due to their relatively simple structure. Alkali atoms have only one valence electron in their outer shell and have a very low ionization potential. The alkali atom Cs have been used to study laser cooling [6] and in atomic clocks developments [7].

In this study we used two-photon two-color on-resonance excitation process on atomic  $^{133}\text{Cs}$ . We investigated the linear polarization spectrum of Cs for the  $6s^2S_{1/2} \rightarrow 6p^2P_{3/2} \rightarrow 10s^2S_{1/2}, 9d^2D_{5/2}$  atomic transitions. The two stepwise excitations are electric dipole allowed transitions. The main idea of this study was to obtain the polarization degree on resonance and in the vicinity of different Ar buffer gas pressures ranging from 50-100 Torr to obtain the polarization spectrum for the collisions between Cs and Ar atoms. We then extracted the disalignment cross section in the  $6p^2P_{3/2}$  excited state using the linear polarization data and a non-linear least-square analysis.

The collisional depolarization cross sections of alkali in excited states interacting with ground state noble-gas atoms have been studied earlier using various

methods ([8–11]). However, only two groups reported a disalignment (collisional depolarization) cross section in the  $6p^2P_{3/2}$  state of Cs with Ar buffer gas. Fricke and Lüscher [8] reported a collisional cross section of Cs  $6p^2P_{3/2}$  state using a significantly different experimental technique. In their study, a Cs-lamp was used and different noble-gases were introduced with pressures up to 30 Torr. A weak magnetic field was used and the collisional frequency between Cs and Ar was restricted by changing the pressure in order to neglect the effects of  $I - J$  coupling in their polarization measurements. Guiry [9] reported a collisional depolarization cross section using both linearly and circularly polarized light with various noble gases, including argon, with pressures ranging from 0-10 Torr. Guiry obtained the polarization data at high magnetic fields ( $\sim 10$  kG) and extracted the cross sections for collisional disorientation and disalignment of the  $6^2P_{3/2}$  cesium atoms. The Hanle effect was used to decouple  $I$  and  $J$  in order to neglect the hyperfine coupling. Also, theoretical calculations for the disalignment cross section of Cs in the excited state in the vicinity of various noble gas atoms have been reported by Okunevich [12] and Rebane [13].

To our knowledge, we report the first collisional depolarization cross section using the two-photon, two-color polarization spectroscopy technique between the excited state Cs atoms and the ground state Ar atoms.

This dissertation is organized as following: In Chapter 2, the theoretical background of the experiment including the concepts of the hamiltonian of the system, the selection rules for the dipole transitions, the fine and hyperfine interactions, the alignment and orientation of the atoms with interaction of light, the linear polarization spectra and the hyperfine depolarization effects on the spectra are presented. Chapter 3 provides information about the experimental apparatus including lasers, optical system and data processing. In Chapter 4 an overview of the experiment is provided. Final discussion, conclusions and brief discussion about the systematic effects are provided in Chapter 5.

# Chapter 2

## Theoretical Background

In this chapter we will discuss the interaction hamiltonian of an atomic system, the selection rules for electric dipole transitions, fine and hyperfine structure of Cs, alignment and orientation of the atom, the linear polarization spectra and the theory of hyperfine depolarization effects on the polarization spectrum.

### 2.1 Hamiltonian of the System

The generation and detection of the fluorescence light involves the interaction between the atom and the electromagnetic waves. In this section we will briefly discuss the Hamiltonian of the system. The properties of this system can be studied with the perturbation theory to degenerate solutions for the Schrödinger equation, which will yield us to the multipolar interaction Hamiltonian of the system. Furthermore, with the electric dipole approximation we will find that the interaction Hamiltonian can be written as the electric-dipole interaction Hamiltonian.

At the end of the 19<sup>th</sup> century it became evident that none of the classical physical laws could apply to the studies of spectroscopy. With the introduction of quantum mechanics, quantitative treatments were possible in the atomic and molecular systems. The motion equation of these systems, which includes both particle and wave properties of the light, was given by Schrödinger.

In classical mechanics the total energy of a particle in a conservative system is given by [14],

$$E = T + V \tag{2.1}$$

where  $T$  is the kinetic energy and  $V$  is the potential energy. For a moving particle along the  $x$  axis of a mass  $m$  and a velocity of  $v$  in a potential field of  $V(x)$  we can write,

$$T = \frac{1}{2}m\left(\frac{dx}{dt}\right)^2 \tag{2.2}$$

$$E = \frac{1}{2}m\left(\frac{dx}{dt}\right)^2 + V(x) = \frac{p^2}{2m} + V(x) \tag{2.3}$$

where  $p$  is the momentum of the particle and

$$v = \frac{dx}{dt}. \tag{2.4}$$

By replacing the momentum in Eq. 2.3 with an operator  $p \rightarrow -i\hbar \frac{d}{dx}$  and multiplying it with a  $\psi$  wave function we obtain the equation in the form of the Schrödinger wave equation:

$$-\frac{\hbar^2}{2m} \frac{d^2\psi}{dx^2} + V\psi = E\psi \quad (2.5)$$

In three dimensions this equation can be written in the following form,

$$\nabla^2\psi + \frac{2m}{\hbar}(E - V)\psi = 0, \quad (2.6)$$

where the laplacian operator  $\nabla^2$  is given by,

$$\nabla^2 \equiv \frac{\partial^2}{\partial x^2} + \frac{\partial^2}{\partial y^2} + \frac{\partial^2}{\partial z^2}. \quad (2.7)$$

If we rearrange Eq. 2.6 we will obtain the following equation

$$\left(-\frac{\hbar^2}{2m}\nabla^2 + V\right)\psi = E\psi, \quad (2.8)$$

or

$$H\psi = E\psi, \quad (2.9)$$

where  $H$  is the Hamiltonian operator,

$$H = -\frac{\hbar^2}{2m}\nabla^2 + V \quad (2.10)$$

The time dependent Schrödinger wave equation is given by,

$$H\Psi = i\hbar d\Psi/dt. \quad (2.11)$$

The time-dependent wave function is

$$\Psi_n(r, t) = \exp(-iE_n t/\hbar)\psi_n(r). \quad (2.12)$$

If we consider the interaction between the atom and the electromagnetic radiation, we can write the complete Hamiltonian for multipolar interactions in Coulomb gauge by replacing the electron momentum by  $p_j \rightarrow p_j + eA(r_j)$ .

$$H = \left(\frac{1}{2m} \sum_j (p_j + eA(r_j))^2\right) + \frac{1}{2} \int \sigma(r)\phi(r)d(r) + \frac{1}{2} \int (\epsilon_0 E(T)^2 + \mu_0^{-1} B^2)dr \quad (2.13)$$

The interaction between the atom and the electromagnetic field is contained in the first part of Eq. 2.13 which involves the vector potential operator  $A(r_j)$  is given by,

$$H_I = \left(\frac{e}{m}\right) \sum_j A(r_j)p_j + \left(\frac{e^2}{2m}\right) \sum_j A(r_j), \quad (2.14)$$

and it is known as the minimal coupling form of the Hamiltonian.

With the unitary transformation we can transform the Hamiltonian from the minimal coupling form to the multipolar form. The transformed multipolar Hamiltonian is

$$\begin{aligned}
H &= \frac{1}{2m} \sum_j \{p_j - e \int_0^1 \lambda r_j \times B(\lambda r_j) d\lambda\}^2 \\
&+ \frac{1}{2} \int \sigma(r) \phi(r) dr + \frac{1}{2} \int (\epsilon_0 E_T^2 + \mu_0^{-1} B^2) dr \\
&+ e \sum_j \int_0^1 r_j E_T(\lambda r_j) d\lambda + \left(\frac{1}{2\epsilon_0}\right) \int P_T(r)^2 dr
\end{aligned} \tag{2.15}$$

The transformation of the Hamiltonian to the minimal coupling form can be found in [15] and the Hamiltonian can be written as,

$$H = H_I + H_R + H_E, \tag{2.16}$$

where  $H_E$  is the Hamiltonian of the isolated atom,

$$H_E = \sum_j \left(\frac{p_j^2}{2m}\right) + \frac{1}{2} \int \sigma(r) \phi(r) dr. \tag{2.17}$$

$H_R$  is the radiation-field Hamiltonian,

$$H_R = \frac{1}{2} \int (\epsilon_0 E_T^2 + \mu_0^{-1} B^2) dr, \tag{2.18}$$

and  $H_I$  is the interaction Hamiltonian between the atom and the electromagnetic field. The sum of four multipolar interaction can be written as

$$H_I = H_{ED} + H_{EQ} + H_{MD} + H_{NL} \tag{2.19}$$

where  $H_{ED}$  is the electric-dipole interaction Hamiltonian,

$$H_{ED} = eD \cdot E_T(0), \tag{2.20}$$

where  $\mu = e \cdot D$  is the dipole moment.  $H_{EQ}$  is the electric quadropole interaction Hamiltonian and can be written as

$$H_{EQ} = \frac{1}{2} e \sum_j (r_j \cdot \nabla)(r_j \cdot E_T(0)) = -\nabla \cdot Q \cdot E_T(0). \tag{2.21}$$

The magnetic dipole interaction Hamiltonian is,

$$H_{MD} = -\left(\frac{e}{4m}\right) \sum_j \{p_j \times B(0) + r_j \times B(0) \cdot p_j\} = \left(\frac{e}{2m}\right) M \cdot B(0), \tag{2.22}$$

where  $M = \sum_j (r_j \times p_j)$  is the sum of electronic angular momentum operators. The final term on the other hand is the nonlinear diamagnetic term

$$H_{NL} = (e^2/8m) \sum (r_j \times B(0))^2 \tag{2.23}$$

which is negligible, since we have linear radiation.

Comparison of the three linear Hamiltonian components shows that the electric-dipole interaction Hamiltonian has a greater magnitude than the magnetic and electric-quadrupole interaction Hamiltonian.

The neglecting of all the other interaction Hamiltonian terms other than the electric-dipole interaction Hamiltonian is known as the electric-dipole approximation. Thus, the total Hamiltonian of the system can be written as

$$H = H_E + H_R + H_{ED}. \quad (2.24)$$

## 2.2 Selection Rules

In this section we will derive the selection rules for the electronic transitions on the levels under study.

In the previous section we showed that with the electric-dipole approximation the interaction Hamiltonian between the atom and the electric field can be written in the form  $H = E \cdot \mu$ . Where  $\mu$  is the electric dipole moment and  $E$  is the electric field of the light which propagates along the laboratory z-axis.

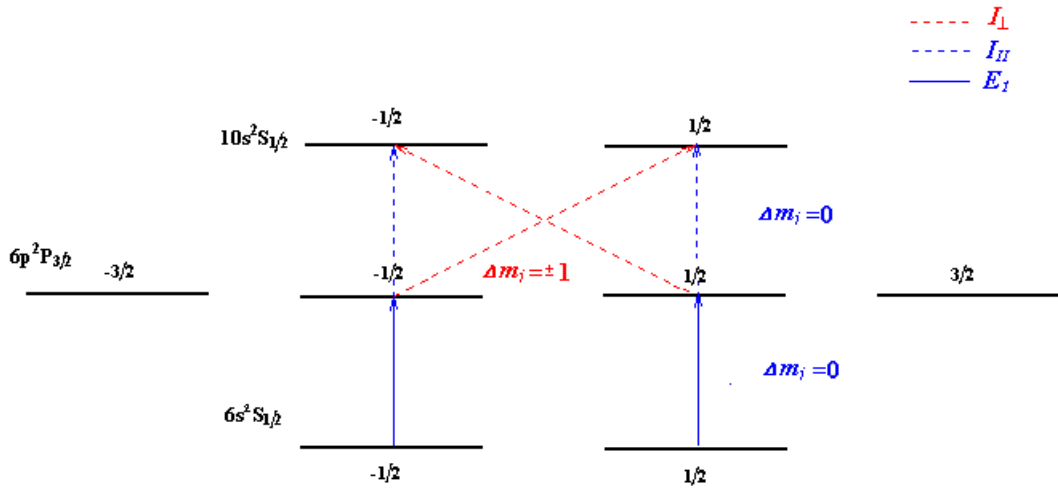


Figure 2.1: Kastler diagram shows the selection rules and relative population on the selected atomic levels for  $I_{\parallel}$  and  $I_{\perp}$ .

The coupling between initial state  $|i\rangle$  and the final state  $|f\rangle$  state by electric dipole moment can be written as,

$$\langle f | \hat{\epsilon} \cdot \vec{r} | i \rangle, \quad (2.25)$$

where  $\vec{r}$  is the position vector of the electron. The electric field of the electromagnetic radiation is,

$$\hat{E}(\vec{r}, t) = E_0(\hat{\epsilon})e^{i(\hat{k}\cdot\vec{r}-\omega t)}, \quad (2.26)$$

where  $\hat{\epsilon}$  is the polarization vector which can be written as,

$$\hat{\epsilon} = \cos\beta\hat{i} + ie^{i\delta}\sin\beta\hat{j}. \quad (2.27)$$

It is useful to define the spherical polar components of the x,y,z axes instead of Cartesian coordinates. Thus,

$$\begin{aligned} r_{-1} &= (\hat{x} - i\hat{y})/\sqrt{2} \\ r_0 &= z \\ r_1 &= -(\hat{x} + i\hat{y})/\sqrt{2} \end{aligned} \quad (2.28)$$

where  $r_{\pm 1}$  corresponds to right and left circularly polarized light,  $r_0$  corresponds to linearly polarized light. For simplicity we will use the symbol  $q$  as a subscript of  $\hat{r}$  to indicate the polarization direction of the light ( $q = 0, \pm 1$ ). Thus, the polarization vector can be written in the following form,

$$\hat{\epsilon}_q = \begin{cases} \frac{-1}{\sqrt{2}}(\cos\beta - \sin\beta) & q=1 \\ 0 & q=0 \\ \frac{1}{\sqrt{2}}(\cos\beta + \sin\beta) & q=-1. \end{cases}$$

The selection rules can be easily found from the Wigner-Eckart (W-E) theorem [16]. The W-E theorem separates the matrix elements of Eq. 2.25 into two parts, the radial and the angular part [6]. Thus the absorption probability of a quantum state with the interaction between the atoms electric-dipole moment and the electric field is given by,

$$\langle j'm'|\hat{\epsilon} \cdot \vec{r}|jm\rangle, \quad (2.29)$$

where  $j', m'$  and  $j, m$  refer to the final and initial state quantum numbers, respectively. The W-E theorem also states that the dependence of the matrix element (Eq. 2.29) on the projection quantum number is contained in the Clebsch-Gordan coefficient as

$$\langle j'm'|r_q^k|jm\rangle = C(jk j'; m q m')\langle j' || r || j \rangle, \quad (2.30)$$

where  $C(jk j'; m q m')$  is the Clebsch-Gordan coefficient and  $\langle j' || r || j \rangle$  is the reduced matrix element which is independent of the quantum numbers  $m$  and  $m'$ . The reduced matrix element contain the properties of the tensor field. For linear polarization where  $q = 1$  and the rank of the tensor matrix for the electric dipole transition which has a line of symmetry  $k = 1$ , the only non-vanishing Clebsch-Gordan coefficient yields the selection rules as  $\Delta j = 0, \pm 1$  and  $\Delta m_j = 0, \pm 1$ . For the linear polarization along the z-axis,  $\Delta m = 0$  when both of the lasers polarization directions are parallel, and  $\Delta m = \pm 1$  when they are perpendicular. The Kastler diagram in Fig. 2.1 shows the allowed transition for our excitation process.

## 2.3 Fine and Hyperfine Interactions

The Cs atom is in the alkali metal group in the periodic table with a nuclear number of  $Z = 133$ .  $^{133}\text{Cs}$  has only one valence electron and can be treated as a hydrogen-like atom. The orbital motion of the valence electron around the nucleus creates an internal magnetic field  $B_L$  which interacts with the electron's magnetic moment and orients its spin. This interaction ( $\vec{\mu}_S \cdot \vec{B}_L$ ) is called the spin-orbit interaction or fine-structure splitting, where the spin ( $\vec{S}$ ) and the orbital angular momentum ( $\vec{L}$ ) combine to form a total angular momentum ( $\vec{J}$ ). Thus, additional energy results from this interaction and the interaction operator can be written as

$$\hat{V}_{FS} = -\vec{\mu}_S \cdot \vec{B}_L \quad (2.31)$$

The interaction Hamiltonian between the spin of the electron and the magnetic field can be written as [17]

$$\begin{aligned} H' &= -\frac{1}{2} \vec{\mu} \cdot \vec{B} = \frac{1}{2} \vec{\mu} \cdot \left( \frac{\vec{v}}{c} \times \vec{E} \right) \\ &= -\frac{\vec{\mu}}{mc} \cdot (\vec{E} \times \vec{p}) \end{aligned} \quad (2.32)$$

where  $\vec{\mu}$  is the magnetic dipole moment,  $\vec{B}$  is the magnetic field,  $\vec{E}$  the electric field and  $\vec{p}$  is the momentum of the electron. In spherical coordinates we can write  $E$  as

$$E_r = -\frac{d}{dr} \phi(r) \quad (2.33)$$

where  $\phi(r)$  is the Coulomb potential.

Substituting Eq. 2.33 into Eq. 2.32 using the relations  $\mu = (\frac{e}{mc}) S$  and  $\vec{L} = \vec{r} \times \vec{p}$ , the spin-orbit interaction Hamiltonian or perturbed Hamiltonian can be written with the *Thomas correction term*, which is a term that has been added to the energy due to kinematic effects as,

$$H' = \frac{1}{2\mu^2 c^2} \frac{1}{r} \frac{dV}{dr} \vec{L} \cdot \vec{S} \equiv f(r) \vec{L} \cdot \vec{S} \quad (2.34)$$

where  $f(r)$  defines a scalar function and it is known as the interaction potential.

We can evaluate the shifting in the energy levels by using  $\vec{L} \cdot \vec{S} = \frac{1}{2} (J^2 - L^2 - S^2)$  since the complete Hamiltonian commutes with the total angular momentum vector operator  $J$  instead of  $L$  and  $S$  [18].

The first order change in energy due to the spin orbit interaction can be calculated as following;

$$\begin{aligned} \Delta E &= \frac{1}{\hbar} \langle E_n^0, l \frac{1}{2} j m | f(r) (J^2 - L^2 - S^2) | E_n^0 \rangle \\ &= [j(j+1) - l(l+1) - \frac{3}{4}] \hbar \int |R_{nl}(r)|^2 f(r) r^2 dr, \end{aligned} \quad (2.35)$$

where  $j$  can take two values,  $j = l \pm \frac{1}{2}$ , for the given  $n$  and  $l$  quantum numbers. The splitting of a level is determined by the interaction potential  $f(r)$ . For an attractive potential, the level  $j = l + \frac{1}{2}$  will be above the level  $j = l - \frac{1}{2}$ .

In order to calculate the magnitude of the energy shifting in a spin-orbit interaction, we need to calculate the interaction potential  $\langle f \rangle$ . Then, an approximate calculation can be done with the hydrogen as

$$\langle f \rangle = \frac{\hbar}{2\mu^2 c^2} Z e^2 \left\langle \frac{1}{r^3} \right\rangle. \quad (2.36)$$

If we estimate for the  $n^{\text{th}}$  orbit and replace  $\left\langle \frac{1}{r^3} \right\rangle \simeq \frac{Z^3}{n^3 a^3}$ , where  $a$  is the Bohr radius of hydrogen  $a = \frac{\hbar^2}{e^2 \mu}$ , we find the following relationship,

$$\begin{aligned} \langle f \rangle &\simeq \frac{\hbar}{2\mu^2 c^2} Z e^2 \left( \frac{Z e^2 \mu}{\hbar^2 n} \right)^3 \\ &\simeq \alpha^2 \frac{Z^4 e^4 \mu}{2n^3 \hbar^3} \\ &\simeq \alpha^2 \frac{Z^2}{n \hbar} |E_n^0|, \end{aligned} \quad (2.37)$$

where  $\alpha$  is the fine splitting constant. Its numerical value is  $\alpha = \frac{e^2}{\hbar c} = \frac{1}{137.037}$  which determines the magnitude in the fine splitting. As you can see from the constant number, the fine splitting in the energy levels are relatively small and the splitting is proportional to the 4<sup>th</sup> power of the nuclear charge  $Z$ .

The internal magnetic field produced at the position of the nucleus due to electronic motions interacts with the magnetic moment of the nucleus resulting a splitting called hyperfine-splitting. The interaction between the magnetic moment of the nucleus and the magnetic field of the electron shells orients the nuclear spin of the atom. The coupling of the angular momentum ( $J$ ) and the nuclear spin ( $I$ ) results to a new total angular momentum ( $F$ ),

$$F = J + I \quad (2.38)$$

where  $F$  can take the values  $F = J + I, J + I - 1, \dots, J - I$ . The hyperfine interaction operator is given as

$$\hat{V}_{HPF} = -\vec{\mu}_I \cdot \vec{B}_J. \quad (2.39)$$

One can calculate the hyperfine interaction energy ( $W_F$ ) using the following [5]

$$W_F = \frac{1}{2} h A K + h B \frac{\frac{3}{2} K(K+1) - 2I(I+1)J(J+1)}{2I(2I-1)2J(2J-1)} \quad (2.40)$$

where  $K = F(F+1) - I(I+1) - J(J+1)$  and  $A$  and  $B$  are the dipolar and quadrupolar coupling constants respectively. The first term of this equation

arises from the interaction between the nuclear magnetic moment and electronic magnetic dipole moments. The second term arises from the interaction between the electronic charge distribution and the electric quadrupole moment. The hyperfine splitting of our study is shown in Fig. 2.2 for the  $6s^2S_{1/2}$ ,  $6p^2P_{3/2}$  and  $10s^2S_{1/2}$  levels that are related to our study. For cesium, the nuclear spin  $I = \frac{7}{2}$  and the coupling constants for each energy level are given elsewhere [5].

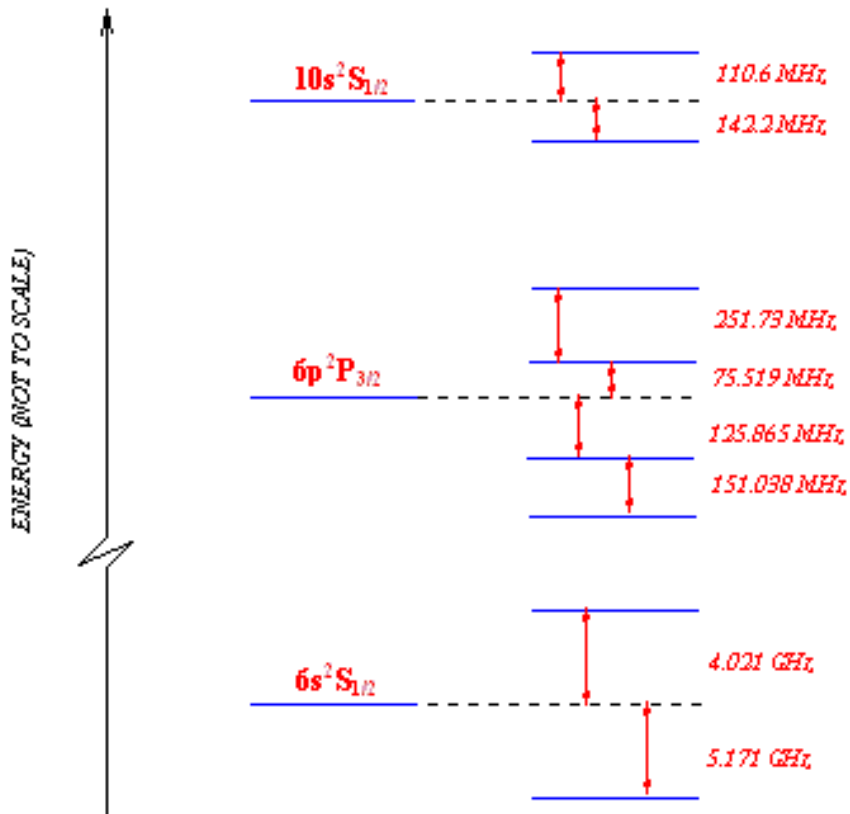


Figure 2.2: Hyperfine splittings of the levels under study.

## 2.4 Orientation and Alignment

Excitation of an atom or molecule by interaction with light in a gaseous medium, leaves the atom in an anisotropic state. To observe the variations of the anisotropy of an atom during the light emission, Fano and Macek introduced the concepts of the alignment and the orientation [19]. The intensity of a radiating system can be measured with the alignment and orientation of the atoms in an excited state. Alignment or orientation of the atoms is a measure of the charge distribution of the levels. The quadrupole moment of an ensemble is called the “alignment” and the dipole moment of an ensemble is called the “orientation”. Fano and Macek, also introduce a general expression of the intensity of polarized light emitted in right-angle geometry, in terms of alignment and orientation and describes the multipole moments of the excited state fragments. Experimentally, the alignment or orientation of an excited state can be determined by measuring the polarization of the final state’s fluorescence.

The most common geometry of an experiment where light interacts with matter is given in Fig. 2.3. As shown in the figure, there are two coordinate frames in interest [20]. The first one is the so called “collision frame” and the second frame is the “detection frame”.

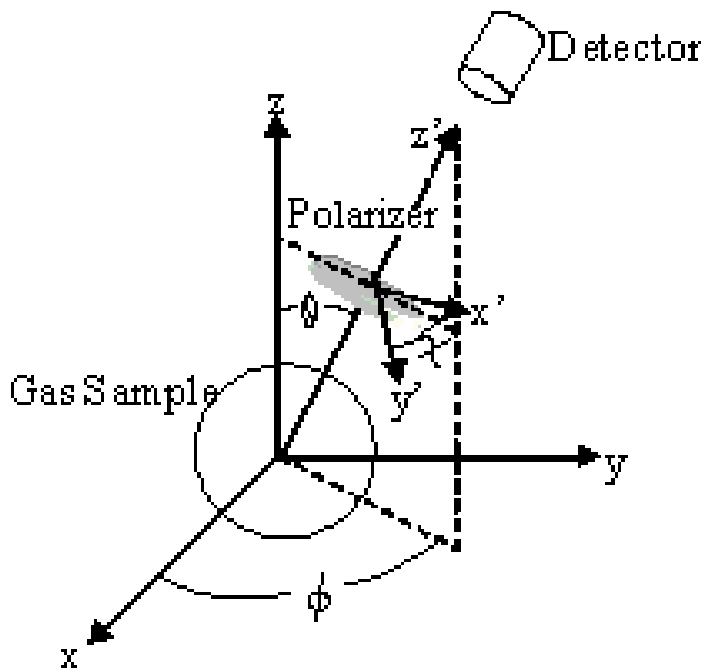


Figure 2.3: Geometry of the collision and detection frame.

The collision frame is adapted to the symmetry of the excitation process of

interest. If we choose the excitation process to be along the z-axis (quantization axis), there will be a cylindrical symmetry about this axis.

The detector frame on the other hand is where the detection of the emitted light takes place. It is free to rotate about the common origin of the two frames. The observation direction of the photon is along the  $z'$  axis, therefore the polarization vector lays on the  $x' - y'$  plane and can be written as,

$$\hat{\epsilon} = \hat{i} \cos(\beta) + \hat{j} \sin(\beta). \quad (2.41)$$

As shown on Fig. 2.3, the orientation of collision frame with its x,y,z coordinates and the detection frame with its  $x', y', z'$  coordinates are defined by the Euler angles  $(\phi, \theta, \chi)$ . Here,  $\theta$  and  $\phi$  are the geometry relating angles between the two frames and  $\chi$  defines the orientation of a linear polarizer placed in the detector frame. The angle  $\beta$  in Eq. 2.41 on the other hand defines the polarization of light to be detected. If  $\beta = 0$  or  $\frac{\pi}{2}$  the light is linearly polarized along the  $x'$  and  $y'$  axis, respectively. For  $\beta = \pm\frac{\pi}{4}$  the polarization of light is circular polarized light.

Thus, the intensity of the fluorescence radiation can be written as [20],

$$\begin{aligned} I(\phi, \theta, \chi) = \frac{1}{3} I_0 \{ & 1 - \frac{1}{2} h^{(2)}(J_i, J_f) P_2(\cos \theta) \langle A_0 \rangle \\ & + \frac{3}{4} h^{(2)}(J_i, J_f) \langle A_0 \rangle \sin^2 \theta \cos 2\chi \cos 2\beta \\ & + \frac{3}{2} h^{(1)}(J_i, J_f) \langle O_0 \rangle \cos \theta \sin 2\beta \}, \end{aligned} \quad (2.42)$$

where  $P_2(\cos \theta) = (\frac{3}{2} \cos^2 \theta - \frac{1}{2})$  is the  $2^{nd}$  rank Legendre polynomial. The other undefined quantities in this formula are the geometrical quantities  $h^{(k)}(J_i, J_f)$ , where  $k=1$  or  $2$ .  $k=1$  represents orientation and  $k=2$  represents alignment. This quantity depends only on the angular momentum quantum numbers of the initial ( $J_i$ ) and final ( $J_f$ ) states.  $\langle A_0 \rangle$  and  $\langle O_0 \rangle$  are the expectation values of the alignment and orientation, respectively.

The alignment can be written as.

$$\langle A_0 \rangle = \frac{\langle 3J_z^2 - J^2 \rangle}{J'(J' + 1)} = \sum_{m'} \frac{|a(m')|^2 [3m'^2 - J'(J' + 1)]}{J'(J' + 1)},$$

and the orientation

$$\langle O_0 \rangle = \frac{\langle J'_z \rangle}{\sqrt{J'(J' + 1)}}.$$

## 2.5 Linear Polarization Spectra

In this section we will apply the concepts of alignment and orientation to the two-color two-photon excitation process of Cs from the  $6s^2S_{1/2}$  ground state to the  $10s^2S_{1/2}$  final state and show the linear polarization degree in terms of alignment.

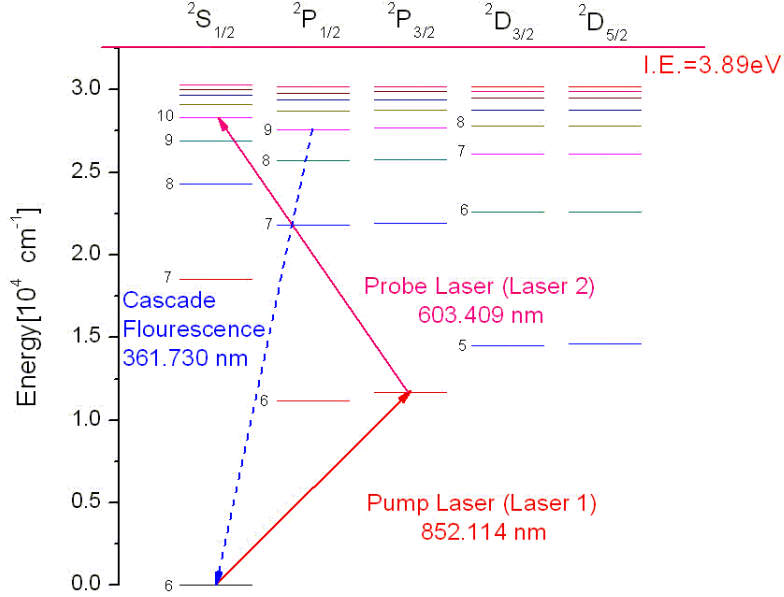


Figure 2.4: Grotrian diagram shows us the excitation and emission scheme in cesium.

For excitation by linearly polarized light source, the detection of the fluorescence from the transition  $J_i \rightarrow J_f$ , two experimental quantities are of interest:

1) The total intensity  $I_0$  with energy  $h\nu$  emitted in all directions, which is proportional to the population on the excited state

2) The linear polarization of the emitted light which is given by  $P_L = \frac{I_{||} - I_{\perp}}{I_{||} + I_{\perp}}$ . The intensities  $I_{||}$  and  $I_{\perp}$  are observed when the polarizer is set at an angle  $\chi = 0, \frac{\pi}{2}$  which is a measure of the alignment of the excited state, respectively.

Excitation with linearly polarized light produces no orientation on the  $6p^2P_{3/2}$  state. Therefore the total intensity of the cascade fluorescence signal depends only on the alignment of the excited state. This reduces the Eq. 2.42 to,

$$I = \frac{I_0}{3} \left[ 1 + \frac{1}{4} h^{(2)}(J, J') \langle A_0 \rangle + \frac{3}{4} h^{(2)}(J, J') \langle A_0 \rangle \cos 2\chi \right]. \quad (2.43)$$

For linear polarization  $\beta = 0$  and for the right angle detection  $\theta = \pi/2$ . For  $\chi = 0$ , we detect the intensity of the cascade fluorescence when both electric field components of the lasers are along the z-axis. Thus parallel intensity is,

$$\begin{aligned} I_{||} &= \frac{I_0}{3} \left[ 1 + \frac{1}{4} h^{(2)}(J, J') \langle A_0 \rangle + \frac{3}{4} h^{(2)}(J, J') \langle A_0 \rangle \right] \\ &= \frac{I_0}{3} [1 + h^{(2)}(J, J') \langle A_0 \rangle]. \end{aligned} \quad (2.44)$$

For  $\chi = \frac{\pi}{2}$ , we detect the intensity of cascade fluorescence when the electric field component of the second excitation is switched from the z-axis to the x-axis. Therefore having the polarization direction of the first laser fixed along z-axis makes laser polarization mutually perpendicular. Thus, perpendicular intensity is,

$$\begin{aligned} I_{\perp} &= \frac{I_0}{3} \left[ 1 + \frac{1}{4} h^{(2)}(J, J') \langle A_0 \rangle + \frac{3}{4} h^{(2)}(J, J') \langle A_0 \rangle (-1) \right] \\ &= \frac{I_0}{3} [1 + h^{(2)}(J, J') \langle A_0 \rangle]. \end{aligned} \tag{2.45}$$

The linear polarization degree in terms of the alignment of the excited state can be found by combining the above equations as,

$$\begin{aligned} P_L &= \frac{I_{II} - I_{\perp}}{I_{II} + I_{\perp}} \\ &= \frac{1 + h^{(2)}(J, J') \langle A_0 \rangle - 1 + \frac{1}{2} h^{(2)}(J, J') \langle A_0 \rangle}{1 + h^{(2)}(J, J') \langle A_0 \rangle + 1 - \frac{1}{2} h^{(2)}(J, J') \langle A_0 \rangle} \\ P_L &= \frac{3h^{(2)}(J, J') \langle A_0 \rangle}{4 + h^{(2)}(J, J') \langle A_0 \rangle}. \end{aligned} \tag{2.46}$$

Eq. 2.46 is very useful in calculating the polarization degree in the absence of collisions. This gives us pure polarization degree for the  $n^2S_{1/2} \rightarrow n^2P_{3/2} \rightarrow n'^2S_{1/2}$  transition in the alkalis.

## 2.6 Hyperfine Depolarization Effects on Polarization Spectra

In the presence of hyperfine splitting, the formulation of intensity has to be modified since the alignment or orientation of the excited state can be changed. There will be some population in the hyperfine levels and the total intensity can then be found as the absolute square summation over all the amplitudes for all possible pathways of the emission. Generally to solve this problem of such non-stationary states we need to solve the time dependent Schrödinger equation. Fano and Macek have found a more simplistic formula for the splitting caused by the hyperfine feature [19–22]. The formula includes a time dependence of the alignment and orientation in the excited state as,

$$\langle A(t) \rangle = \langle A(0) \rangle g^{(k)}(t) \tag{2.47}$$

and

$$\langle O(t) \rangle = \langle O(0) \rangle g^{(k)}(t). \tag{2.48}$$

For the excitation to  $6p^2P_{3/2}$  with a linearly polarized light source, the orientation does not play a role as we mentioned in section 2.5. Thus, we are interested in the time dependence of the alignment.

The hyperfine depolarization coefficient can be written as [1]

$$g^{(k)}(t) = \sum_{F, F'} \frac{(2F+1)(2F'+1)}{(2I+1)} \left\{ \begin{array}{ccc} F & F' & k \\ J & J' & I \end{array} \right\} \cos w_{F'F} t$$

where  $w_{(F'F)}$  is the frequency splitting between two hyperfine levels.

The depolarization coefficient, depending on the precession time of  $\vec{J}$  about  $\vec{F}$ , can affect the excited state. If the coupling time of  $\vec{I}$  and  $\vec{J}$  is so slow that no precession about F occurs before the atom is excited from the  $6p^2P_{3/2}$  to the final state  $10s^2S_{1/2}$  or  $9d^2D_{5/2}$ , the depolarization coefficient will not have any effect on the observed intensity. In other words  $g^{(k)} = 1$ , and the unresolved oscillations have no depolarization effect. If  $\vec{J}$  precesses many times or even completes one full circle of precession about  $\vec{F}$  before the light is emitted from the intermediate state, the alignment will change since  $g^{(k)} \neq 1$ . This states the time dependence of the alignment. In other words, as  $t$  becomes greater than zero,  $\vec{J}$  and  $\vec{I}$  precess about  $\vec{F}$  and the  $g^{(k)}$  factor decreases from its maximum value of 1. The depolarization coefficient of the levels we are interested in this study are calculated elsewhere [1].

The linear polarization degree with the hyperfine depolarization effect can be found by substituting the the time dependent alignment and the depolarization coefficient into Eq. 2.46 to get:

$$P_L = \frac{3h^{(2)}(J, J') \langle A_0 \rangle g^{(k)}}{4 + h^{(2)}(J, J') \langle A_0 \rangle g^{(k)}} \quad (2.49)$$

In addition, there is a technique to minimize the hyperfine depolarization effect which is called the ‘‘pump-probe’’ technique. If the overlap time of the pump and probe laser pulses are shorter than the inverse of the greatest hyperfine frequency component ( $\frac{1}{\omega_{F'F}} = t_{F'F}$ ) in the intermediate state, we can excite the atom to the final state before J and I couples and completes a full cycle of precession about F. This would freeze the electronic alignment and give us a polarization degree without any hyperfine depolarization effect.

# Chapter 3

## Experimental Apparatus

In this section you will find a detailed description of the characteristics of the experimental setup and optical systems. Fig. 3.1 shows an overview of the experimental apparatus. This section is subdivided into four: Lasers, Polarization of Light, Oven and Cell, Detection of the Signal and Data Processing.

### 3.1 Lasers

We use a Continuum Surelite state-of-the art Nd:YAG (neodymium doped yttrium aluminum garnet) pulsed laser running with the second harmonic generator at 532 nm. The repetition rate of the laser is 20 Hz with a pulse width of 4-6 ns. The YAG average power at the exit port is 4.5 W. The pumping scheme of our experiment is shown in Fig. 3.2. The YAG laser beam is directed to the dye laser apparatus by three beam splitters. All of the beam splitters are antireflective (AR) coated on one side (CVI W1-PW1-1012-C-532-45UNP) to prevent ghost reflections entering the laser cavity. Each of them passes approximately 9% of the YAG power. The average power of the YAG laser after the first and second beam splitter is 0.2 W and 0.18 W respectively. The YAG average power is measured by using a power meter (Molelectron Detector Inc., PowerMax PM10V1) which has a maximum pulse energy density resistance of 5 J/cm<sup>2</sup> (1 GW/cm<sup>2</sup>).

The dye lasers, pumped by Nd:YAG, are constructed in the Littman-Metcalf cavity design at grazing incidence to achieve a wide tunability range and narrow bandwidth [23]. The geometry of the grazing incident dye laser cavity design is shown in Fig. 3.3. The cavity of the dye lasers consists of grating, dye cell, cylindrical lens, tuning mirror and an output coupler. As shown in the figure, the dye cell is tilted to avoid reflections from the back surface of the cell.

The dye laser 1 (pump laser), which excites the first transition of Cs from the  $6s^2S_{1/2}$  to the  $6p^2P_{3/2}$  uses an organic dye LDS 867 (Exciton Inc.) which was diluted with methanol. The concentration of the oscillator is 84 mg/L. The output wavelength of the dye is at 852.112 nm and its tunability range is from 830nm to 920 nm. We used a dye flowing system to stabilize the power of the pump laser. The average output power is approximately 3.0 mW.

The dye cell of the dye laser 1 is an AR coated flow cell (NSG Precision Cells

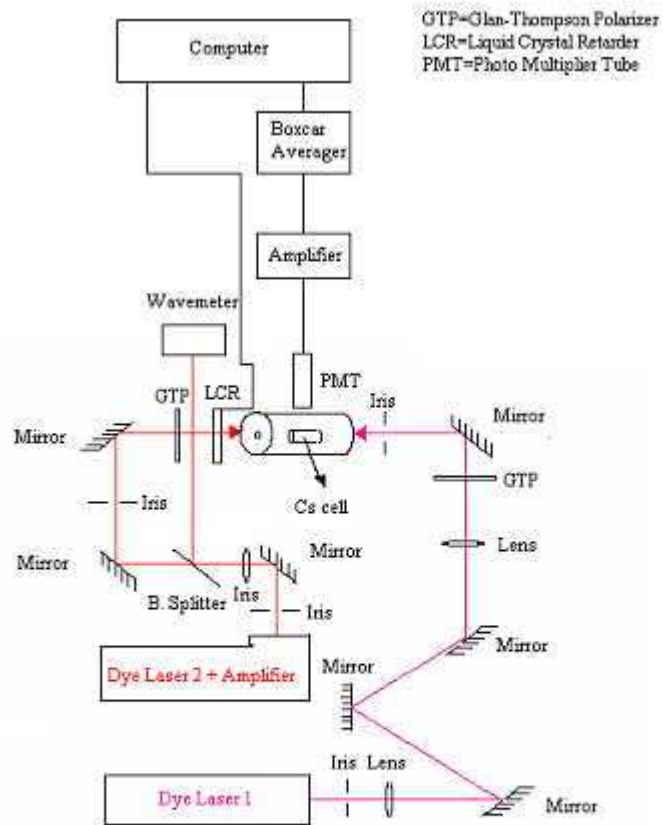


Figure 3.1: Schematic overview of experimental apparatus.

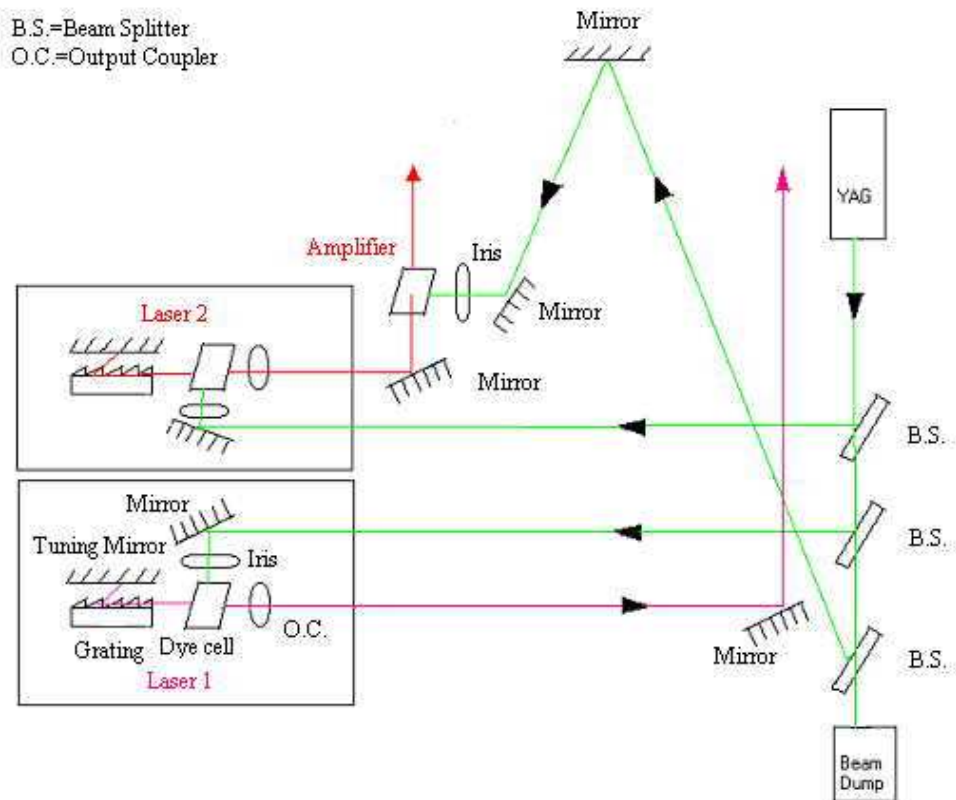


Figure 3.2: Pumping scheme of the experiment.

Inc., T-524) with a capacity of 2 ml. It is made of quartz and its light path is 8 mm. We used a dye circulator (Spectra Physics, Model 376) to have a continuous flow of the dye into the flow cell in order to stabilize the power of the laser. The grating that we used in the oscillator cavity is a 30x30 mm gold coated (Edmund Industrial Optics, Y55-261) grating which has 1200 grooves/mm. It has an efficiency of 75% at a blaze wavelength of 750 nm. The output coupler is a wedged window (CVI, LW-2-1037-C) which prevents interference between the reflections from the front and back surfaces. The cylindrical lens has a focal length of 5.08 cm and it focuses the YAG laser at the edge of the dye cell to avoid heating of the dye. The tuning mirror used in the cavity is a broadband mirror (Thorlabs Inc., BB1-E03) with 99.9% reflectivity in the 750-1150 nm range. It is mounted on a precision mount for tuning the laser to a desired wavelength.

The dye laser 2 which excites the Cs atoms from the  $6p^2P_{3/2}$  to the  $10s^2S_{1/2}$  uses rhodamine 640 perchlorate (Exciton Inc.), and is also diluted with methanol. We used an oscillator and amplifier medium the dye laser 2. The oscillator concentration is 141.8 mg/L. For the  $6p^2P_{3/2}$  to  $9d^2D_{5/2}$  excitation, we used rhodamine 610 perchlorate (Exciton Inc.) with an oscillator concentration of 141.8 mg/L. The dye concentrations of the lasers were selected from Exciton catalog. The wavelength tunability range of the laser is in the visible region, 580-650 nm. We built an amplifier to amplify the power of the dye laser 2. The amplifier uses rhodamine 640 perchlorate with a concentration of 18.9 mg/L for the final  $10s^2S_{1/2}$  excitation state. For the  $9d^2D_{5/2}$  state, the amplifier uses a dye concentration of 18.9 mg/L. The average power before and after the amplifier is 0.2 mW and 4.8 mW respectively. The powers of the dye laser are measured by using a power meter (Molelectron Detector Inc., PowerMax PS19), which has a maximum pulse density resistance of 50 mJ/cm<sup>2</sup> (1 MW/cm<sup>2</sup>).

For the dye laser 2 oscillator and amplifier we used a quartz AR coated dye cell (T-509) which has a capacity of 3.2 ml and a light path of 8 mm. The grating is a holographic grating (Edmund Industrial Optics, Y43-215) for the visible region and has a size of 12.5 x 25 mm with 1200 grooves/mm with efficiency of 55%. We used similar cylindrical lens and output coupler as the one in the dye laser 1 cavity. The mirror, used in the cavity is a broadband mirror (Thorlabs Inc., BB1-E02) which has a 99.7% reflectivity in the 400-900 nm range. It is mounted on a kinematic mirror mount (Newport, 610 Series), which has a coarse and a fine adjustment knob for vertical and horizontal axes. The horizontal fine scale is replaced with a motor driver (Ardel Kinematic Corp, Motor Mike) to tune the laser remotely. Each motor driver step corresponds to a 0.01 nm change in the wavelength. The tuning curve of dye laser 2 is illustrated in Fig. 3.4.

The wavelength of the lasers is measured by a wavelength meter (Coherent, WaveMaster), which operates in a 380-1095 nm wavelength range with an accuracy of approximately 0.001 nm. It has a power resistance of 100 mW.

The free spectral range of the lasers cavity is calculated by using the following equation,

$$FSR = \frac{c}{2nd}, \quad (3.1)$$

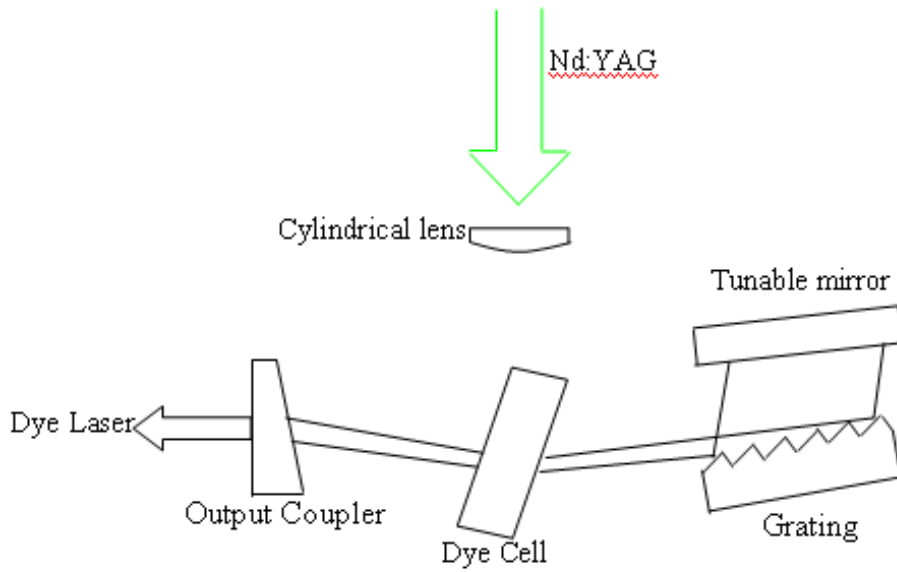


Figure 3.3: Littman-Metcalf cavity with grazing incidence design.

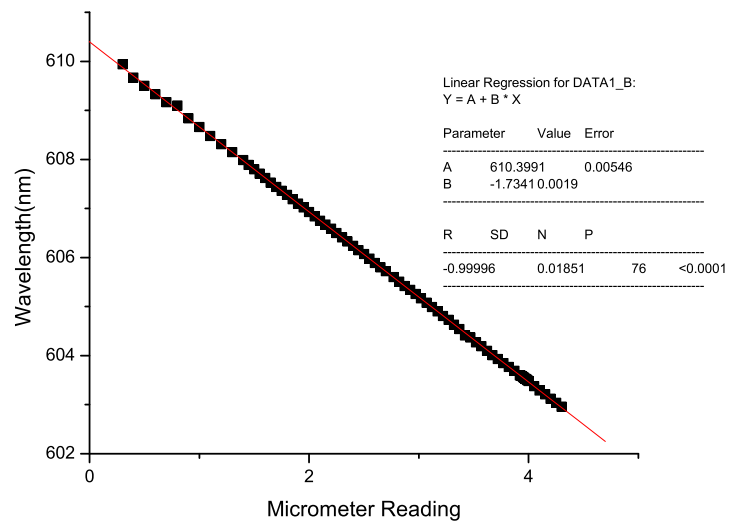


Figure 3.4: Micrometer tuning curve.

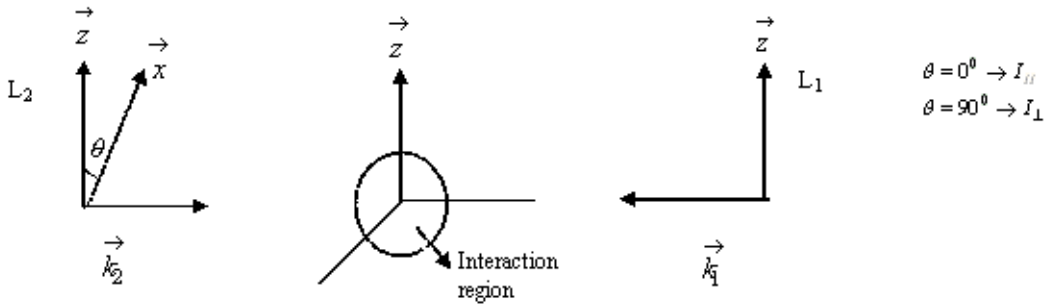


Figure 3.5: Geometry of the Experiment.

where  $d$  is the cavity length,  $c$  is the speed of light and  $n$  is the index of refraction. The FSR of dye laser 1 and dye laser 2 cavities was calculated as 1.05 GHz and 0.9 GHz, respectively.

As shown in Fig. 3.1, we used irises after the output of dye laser 1 and dye laser 2 amplifier to eliminate unwanted light and to pick up the center portion of the laser beams. All mirrors used in lasers paths are dielectric mirrors (Thorlabs Inc., BB1-E03 and BB1-E02) chosen for their specific reflectivity wavelength range.

### 3.2 Polarization of the Light

The Nd:YAG laser is  $> 95\%$  vertically polarized. The cavity of the dye laser does not change the characteristic polarization of the pump laser. Thus, the output beam of both dye lasers is vertically polarized along a laboratory z-axis. We used Glan-Thompson (Thorlabs Inc., GTH10M) polarizers in both laser paths in order to purify and to achieve a higher degree of polarization. The contrast ratio of Glan-Thompson polarizers is 1:100,000. The geometry of our experiment is shown in Fig. 3.5.

The dye laser beams propagate collinearly, are aligned and overlap in the center of the oven where the Cs cell is located. We checked the overlapping of the beams by using an infrared card while blocking and unblocking each laser beam. This was done before they entered the oven from both sides of the oven windows as shown in Fig. 3.1. After ensuring that the dye lasers were vertically polarized with the Glan-Thompson polarizers, we used a Liquid Crystal Variable Retarder (LCVR) (Meadowlark Optics, D3040) in the laser 2 path to alternate the polarization direction of the dye laser 2 parallel and perpendicular to that of the dye laser 1. This procedure was done in order to achieve the polarization spectrum of Cs for the  $6s^2S_{1/2} \rightarrow 6p^2P_{3/2} \rightarrow 10s^2S_{1/2}$  transition.

The LCVR consist of a cavity which is filled with nematic type liquid crystal molecules. Nematics have common axis of alignment and their optical axis can be rotated with weak external agents. Electrical components are attached to the cavity and it is connected to an interface to remotely control the alignment of the nematics. By applying a certain voltage to the LCVR we can change the slow

and fast axis to achieve a sought polarization of dye laser 2. We can change the polarization direction of dye laser 2 to perpendicular (along x-axis) by applying a voltage of  $\sim 2$  V and to parallel (along z-axis) by applying a voltage of  $\sim 7$  V. We mounted the LCVR on a high precision rotation mount (Thorlabs Inc., PRM1) to attain a high level of polarization, precision.

We used a following procedure to check the contrast ratio of LCVR: A photo diode was located after the Glan-Thompson polarizer which was used to polarize the dye laser 1. It was connected to an oscilloscope (HP, 5422 A) to screen the intensity of the incoming light. As shown in Fig 3.1, dye laser 2 passes through the Glan-Thompson polarizer and the oven and through the second Glan-Thompson polarizer into the photo diode. The dye laser 1 beam was blocked during this measurement. We attenuated the dye laser 2 beam by using various neutral density filter to prevent saturation of the photo-diode. The LCVR is remotely controlled by a computer driver software program (Meadowlark Optics, Cell Drive 3000) which changes the voltage to obtain the sought polarization. We adjusted the voltage of the LCVR so that the polarization of the dye laser 2 beam was perpendicular to the second Glan-Thompson polarizer (GTP). Since the photo diode was placed right after the second GTP, we could observe the optimum voltage for the LCVR by watching the intensity of dye laser 2 beam on the oscilloscope. We changed the voltage until the intensity signal reached the minimum. Fine adjustments were done by slightly rotating the LCVR with its high precision mount to obtain a higher degree of polarization. The contrast ratio of dye laser 2 was then calculated by taking the ratio of the observed maximum and minimum intensities on the oscilloscope. The extinction ratio of the LCVR was measured about 1:8,000.

The procedure of checking the contrast ratio of the LCVR was done before each data processing. The optimum voltage value for the LCVR was than used in a LabVIEW program (National Instruments, LabVIEW 7.0 Software) and its DAQ board (National Instruments, PCI 1200) to obtain the polarization spectrum.

### 3.3 Oven and Cell

The oven is made of aluminum and has a cylindrical shape with two windows to allow the lasers entrance. The dye lasers propagate in opposite directions as shown in Fig. 3.1. The detection of the fluorescence signal is obtained from the third window which is perpendicular to the propagation direction of the lasers. The oven windows have a diameter of 1.27 cm. The photographs of the oven and cell are shown in Fig. 3.6-3.8.

The cesium cell, made of pyrex, is mounted at the center of the oven. The cell has a cylindrical shape and it is aligned with the end windows of the oven. The length of the cell is 5.08 cm inches and has a diameter of 2.54 cm. We also mounted a concave mirror inside the oven near the Cs cell on the opposite direction of the observation window. This was used to minimize the loss of the fluorescence signal emitting to other directions. We collect more signal with this mirror at the detection site. A K type thermocouple (Omega, KMQSS-020U-60) is attached to the cell for monitoring the temperature of the cell. The oven is wrapped with a

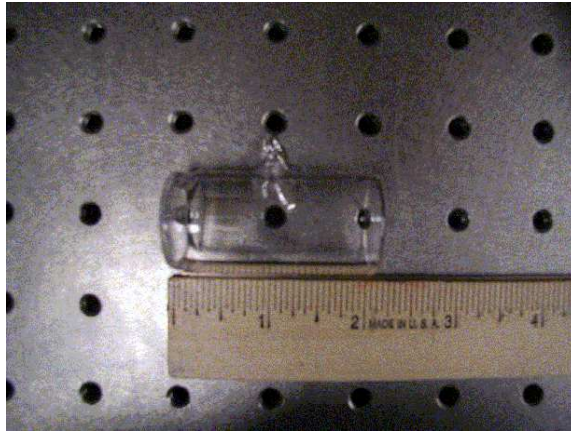


Figure 3.6: Cesium Ccell.



Figure 3.7: Oven with Cs cell inside.

flexible flat heavy insulated samox type electric heating tape (Cole Palmer, 36050-20). We used fiber flax to cover the oven and wrapped aluminum foil around it in order to isolate the oven and maintain a uniform temperature. The thermocouple and the heating band are connected to a temperature controller (Cole Palmer, Digi-Sense EW-89000-00) to stabilize the temperature of the cell. The temperature controller has an accuracy of  $\pm 0.1^{\circ}\text{C}$ .

Our cells contain pure Cs atoms and Cs atoms with Ar pressures at 5 Torr, 30 Torr, 60 Torr and 100 Torr. The vapor density in the cells range from  $\sim 10^{10}\text{atoms}/\text{cm}^3$  to  $10^{15}\text{atoms}/\text{cm}^3$  in a temperature range from  $25^{\circ}\text{C}$  to  $200^{\circ}\text{C}$  respectively. Fig. 3.9 shows the vapor-pressure curve of Cs with the Cs density at different temperatures.



Figure 3.8: View of the side and end windows of the oven.

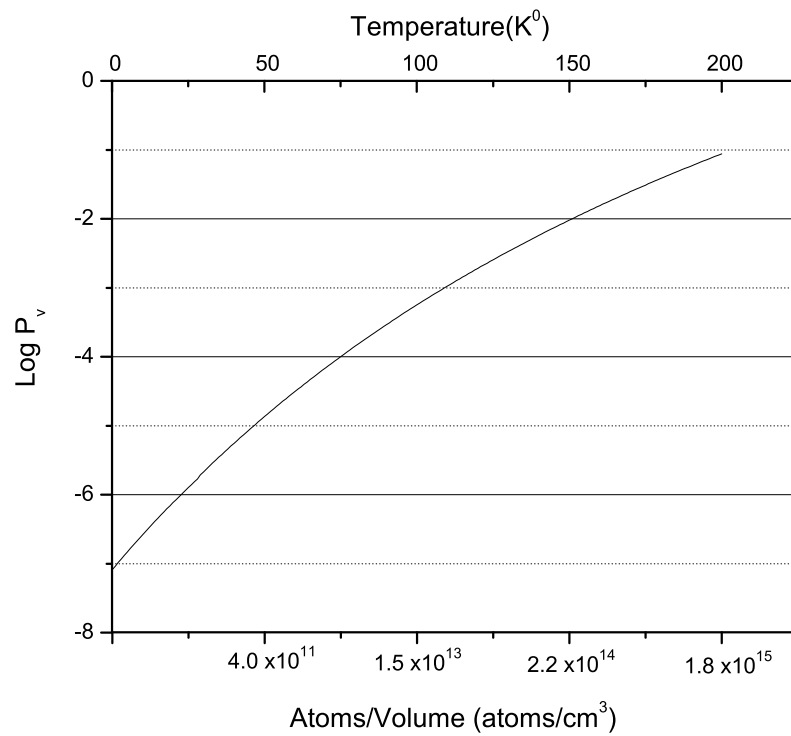


Figure 3.9: Vapor pressure curve of Cs.

### 3.4 Detection of the Signal and Data Processing

A photo multiplier tube (PMT) is placed at the side window of the oven to detect the cascade fluorescence. The PMT tube (Hamamatsu, R955) is a side-on tube with a spectral response range of 160-900 nm and it has a quantum efficiency of 29% at 220 nm. It is operated at 800 V with a high power supply (Stanford Research Inc., PS350). For the  $6s^2S_{1/2} \rightarrow 10s^2S_{1/2}$  transition the combination of a colored-glass filter (Coherent, UG11) and an interference filter (Coherent, 35-3045-000) was placed in front of the PMT to detect cascade fluorescence from  $9p^2P_{1/2} \rightarrow 6s^2S_{1/2}$ . The peak transmission wavelength of the interference filter, which passes 31% of the desired wavelength, is at 366.7 nm and has a FWHM of 10.7 nm. The colored glass filter was used to cut the scattered YAG and laser light. For the  $6s^2S_{1/2}$  to  $9d^2D_{5/2}$  transition, an interference filter with a FWHM of 10.3 nm (Coherent, 35-3003-000) and a peak transmission wavelength of 350.5 nm which passes 32% of the desired wavelength is used, in order to detect the fluorescence from the  $10p^2P_{3/2}$  to  $6s^2S_{1/2}$ . The output signal from the PMT was sent to a three-stage amplifier (Stanford Research Inc., SR240). Each stage amplified the signal by a factor of 5. We used a 50-ohm coaxial cable between the stages and sent the amplified signal to a boxcar averager/integrator (Stanford Research Inc., SR250). The boxcar was triggered by YAG pulses which was picked up by a glass slide and sent to a photo diode. It was then connected to the averager. Monitoring the output signal on the oscilloscope and adjusting the gate width simultaneously determined the gate width. The gate width of the boxcar averager was set to 900 ns to detect only the signal within the gate width without noise. The sensitivity voltage of the boxcar averager/integrator was proportional to the input signal. We used the last sample output of the boxcar averager. This allows us to have a shot by shot analysis of the signal. The output was then sent through a outbreak box (National Instruments, CB-68LP) to a Data Acquisition board (DAQ) (National Instruments, PCI 6014) which converts the analog signal to digital signal. The digital signal was then accumulated and processed by a LabVIEW program (National Instruments, LabVIEW 7.0). The LabVIEW program remotely controls the polarization switch and the frequency scan of the dye laser 2. The wavelength was remotely scanned within a range of 603.1-603.9 nm. The stepper motor was also remotely controlled by the LabVIEW program and was moved 75 steps to complete one polarization run. For each step, the polarization direction of dye laser 2 was changed perpendicular and parallel to the polarization direction of dye laser 1. Each step of the stepper motor refers to a wavelength change of approximately 0.01 nm. The polarization data taken at each frequency is the average of 1000 data points.

The data was saved on an excel sheet by the program. To analyze the polarization data, we used Origin (OriginLab., Origin 7.5). We plot the data and analyzed the polarization degree on resonance. The polarization degree was found with the following formula,

$$P_L = \frac{I_{II} + I_{\perp}}{I_{II} - I_{\perp}} \quad (3.2)$$

where  $I_{II}$  and  $I_{\perp}$  are the measured intensities when both lasers are parallel ( $I_{\parallel}$  and

perpendicular ( $I_{perp}$ ) to each other.

# Chapter 4

## Overview of the Experiment

In this section you will find an overview of the details of the experiment as well as information about the LabVIEW program that we used to interpret and analyze the polarization data.

The polarization spectrum of the  $6s^2S_{1/2} \rightarrow 6p^2P_{3/2} \rightarrow 10s^2S_{1/2}$  was measured by using a two-color two-photon excitation process in atomic cesium. A picture of the experimental apparatus is shown in the Appendix C.1. The polarization degree of the final atomic level was measured by using two dye lasers at resonance frequencies. The dye laser's wavelengths on resonance for the  $6s^2S_{1/2} \rightarrow 6p^2P_{3/2} \rightarrow 10s^2S_{1/2}$  are 852.112 nm and 603.409 nm. The photographs of the dye lasers wavelengths for the on resonance excitation  $6s^2S_{1/2} \rightarrow 6p^2P_{3/2} \rightarrow 9d^2D_{1/2}$  were 852.112nm and 584.434 nm. The dye lasers in Littman-Metcalf cavity design are shown in C.2, C.3, C.4 and C.5.

Detection of fluorescence from the  $10s^2S_{1/2}$  state was achieved from the  $9p^2P_{3/2}$  to the  $6s^2S_{1/2}$  ground level. Since  $10s^2S_{1/2} - 6s^2S_{1/2}$  transition is forbidden, we observed the cascade fluorescence from the  $9p^2P_{1/2}$  state to the  $6s^2S_{1/2}$  state. Similarly, the detection from the  $9d^2D_{5/2}$  state was observed from the  $10p^2P_{3/2}$  to the  $6s^2S_{1/2}$  state. The fluorescence was then detected by a PMT at a  $90^\circ$  angle which was placed at the detection window of the oven. To make sure that our first laser was on resonance, we placed an interference filter in front of the PMT to obtain the fluorescence signal of the first excitation process. We monitored the signal of the first excitation process on the scope and then tuned the laser 2 to resonance. The signal from the two-photon excitation process was then detected by using an interference filter to observe the fluorescence signal at 361.730nm for the  $6s^2S_{1/2} \rightarrow 10s^2S_{1/2}$  transition and 347.826 nm for the  $6s^2S_{1/2} \rightarrow 9d^2P_{5/2}$  transition as described in section 3.4.

Both of the dye lasers were polarized along the arbitrary z-axis by use of Glan-Thompson Polarizers before they entered the oven, as shown in C.6. The polarization direction of the second laser was then switched remotely via a Liquid Crystal Retarder.

The signal from the PMT was sent to an amplifier, shown in C.7, then to a DAQ board which was connected to a computer as shown in C.8.

Fig. B.1 in the appendix section shows the front panel of the control program

that we used to take the polarization data. It includes the stepper motor subVI to scan the probe laser of our excitation process within a  $\pm 11\text{cm}^{-1}$  range and a subVI for the LCR to switch the polarization back and forth remotely.

Fig. B.2 shows a sequence in the block diagram of the LabVIEW program and it includes the program to control the stepper motor. In Fig. B.3, the subVI of the stepper motor is shown. By applying a certain voltage we can change the movement of the stepper motor from fine to coarse and can arrange the wavelength scan for each tune.

The alignment of the laser beams before they entered the oven was checked. Also, the contrast ratio of the LCR was measured by using a photo diode and optical density filters. To achieve a better degree of polarization, we used the interface of the LCR, shown in Fig. B.4. We placed a photo-diode on the laser 2 beam after it passed through the LCR. By monitoring the intensity of the laser beam on the scope we changed the applied voltage on the LCR by using the interface. The optimum voltage for the perpendicular and parallel case was then entered into the LabVIEW programs shown in Fig. B.5 and B.6. The optimum set voltage was connected to the subVI of LCR, shown in Fig. B.7.

By reading the wavelength from the wave meter we entered the starting wavelength and the range of the scan on the front panel of LabVIEW. Each data point for each frequency whether the polarization is parallel or perpendicular is an average of 1000 data points. The polarization dependent intensity data was then saved as excel files by the LabVIEW program. The data were then analyzed by an Origin lab program and the polarization degree was extracted from the data.

Before each data taking process, the powers of the YAG and the dye lasers were measured. The dye of the laser 2 oscillator and amplifier were refreshed in a weekly basis. This basis was not required for laser 1 since we used a dye flowing machine, which allowed us to have a continuous flow from a dye container with a capacity of 500 ml into the dye cell. The container with the dye was placed into another container filled with cold water to cool the flowing dye in order to reduce the heating due to the friction of the dye with the dye flowing tube.

These procedures we briefly described were done on an every day basis before taking the polarization spectrum.

# Chapter 5

## Results

### 5.1 Data and Analysis

In this section, the results of the stepwise two-photon linear polarization spectrum of Cs in the  $6s^2S_{1/2} \rightarrow 6p^2P_{3/2} \rightarrow 10s^2S_{1/2}, 9d^2D_{5/2}$  transitions are presented. Also, the collisional depolarization of the excited state in the presence of Ar buffer gas and the disalignment cross section of the intermediate states are presented.

### 5.2 Overview of the Measurements

The general experimental scheme is illustrated in Fig. 5.1. We used on resonance two-photon two-color pump-probe technique. Then, the linear polarization spectrum was obtained. The cascade fluorescence on the  $9d^2D_{5/2}, 10s^2S_{1/2} \rightarrow 6s^2S_{1/2}$  transitions were detected by a PMT with an interference filter for each transitions. The signal from the PMT was than amplified by a gated integrator and sent to data acquisition board and stored in a computer for analysis. Specifications of the lasers and transitions are given in Table 5.1. Laser 1 (pump laser) is linearly polarized along a laboratory z-axis, while the polarization of laser 2 (probe laser) was controlled by a liquid-crystal variable retarder to be either along or perpendicular to the z-axis.

The frequency of the first dye laser was fixed on resonance while the second is changed within a  $\pm 11\text{cm}^{-1}$  range over the  $10s^2S_{1/2}$  and  $9d^2D_{5/2}$  state.

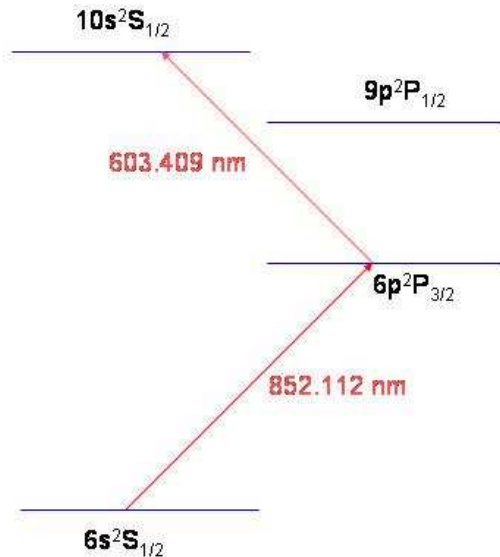


Figure 5.1: Energy level diagram for selected excited electronic states in atomic Cs. The figure also shows the approximate air wavelengths of the two-pulse laser light sources. The cascade fluorescence from the  $9p^2P_{1/2}$  to  $6s^2S_{1/2}$  is detected.

### 5.3 Linear Polarization Measurements

The measurements of the linear polarization degree are obtained. Fig. 5.2 and Fig. 5.3 show typical spectra for the  $6s^2S_{1/2} \rightarrow 6p^2P_{3/2} \rightarrow 10s^2S_{1/2}, 9d^2D_{5/2}$  transitions at  $70^{\circ}C$ . In the  $6s^2S_{1/2} \rightarrow 9d^2D_{5/2}$  transition scan, there is a second peak, which comes from the close lying state of  $9d^2D_{3/2}$  at  $584.709$  nm. Since we scan the spectrum within  $\pm 11cm^{-1}$  range we observe the fluorescence from this state as well. We are interested in obtaining the polarization degree in the  $9d^2D_{5/2}$  state, therefore our measurements does not include the analysis for the  $9d^2D_{3/2}$  peak. The background signal was subtracted from the parallel and perpendicular signals in order to have a more accurate measurement of the polarization spectra. The polarization data taken at each frequency is the average of 1000 data points. The  $I_{\parallel}$  and  $I_{\perp}$  signals from the on-resonance polarization spectrum were extracted to calculate the linear polarization degree. The final polarization degree was found by taking the average of several polarization data, and the statistical error was found by taking the standard deviation of each scan.

In the absence of Ar buffer gas, the polarization degree of the two-photon polarization process in the  $6s^2S_{1/2} \rightarrow 6p^2P_{3/2} \rightarrow 10s^2S_{1/2}, 9d^2D_{5/2}$  can be calculated either from Eq. 2.30 using the Wigner -Eckhart theorem or from Eq. 2.46.

Table 5.1: Specifications of the lasers we used in the experiment.

$P_{YAG}$	1.85W
$P_{L_1}$	5.8mW
$P_{L_2}(\text{oscillator})$	2mW
$P_{L_2}(\text{amplifier})$	5.6mW
$6s^2S_{1/2} \rightarrow 6p^2P_{3/2}$	852.112nm
$6p^2P_{3/2} \rightarrow 10s^2S_{1/2}$	603.409nm
$6p^2P_{3/2} \rightarrow 9d^2D_{5/2}$	584.434nm
$6p^2P_{3/2} \rightarrow 9d^2D_{3/2}$	584.709nm
$9p^2P_{1/2} \rightarrow 6s^2S_{1/2}$	361.730nm
$10p^2P_{3/2} \rightarrow 6s^2S_{1/2}$	347.826nm
$L_1$	84 mg/L(Methanol)
For 10S $L_2(\text{oscillator})$	114 mg/L(Methanol)
$L_2(\text{amplifier})$	16.83 mg/L(Methanol)
For 9D $L_2(\text{oscillator})$	141.8 mg/L(Methanol)
$L_2(\text{amplifier})$	18.9 mg/L(Methanol)
Gatewidth	900ns

The Clebsch-Gordan coefficients for the related transitions are given in Appendix A. Thus, in the absence of buffer gas and with no hpf depolarization effect, the calculated polarization degree for the  $6s^2S_{1/2} \rightarrow 10s^2S_{1/2}$  excitation is 60% and  $6s^2S_{1/2} \rightarrow 9d^2D_{5/2}$  excitation 14.28%. Taking hpf depolarization effect into account, the calculated polarization degree for the  $10s^2S_{1/2}$  state is 15.6% and for the  $9d^2D_{1/2}$  state is 3.25%. The measured polarization degree we found from the experiment for the  $10s^2S_{1/2}$  state and  $9d^2D_{5/2}$  state is 15.76%(3%) and 3.71%(1.3%), respectively. Thus, our results are in excellent agreement with theory.

It is possible to use a pump-probe technique to minimize the hyperfine depolarization effect on the polarization degree. In this case, the overlap time of the pump-probe dye lasers must be smaller than the inverse frequency of the highest hyperfine splitting in the  $6p^2P_{3/2}$  intermediate state so that the hyperfine interaction will not have time to occur before this state is excited to final state by the second laser. The shortest precession time in the excited state hyperfine levels of  $^{133}\text{Cs}$  is about 3ns. We shorten the overlap time of the two dye lasers in order to minimize this effect. Since we have no information of the shape of the pulses we recalculated the expected polarization degree of the  $10s^2S_{1/2}$  and  $9d^2D_{5/2}$  states, by using the Eq. 2.49. A comparison of the calculated polarization degree with and without hyperfine depolarization effects and our measured polarization degree can be found in Table 5.2. Our measured values are in excellent agreement with polarization degree due to the dependence of the  $g^{(2)}$  hyperfine depolarization coefficient given by [1].

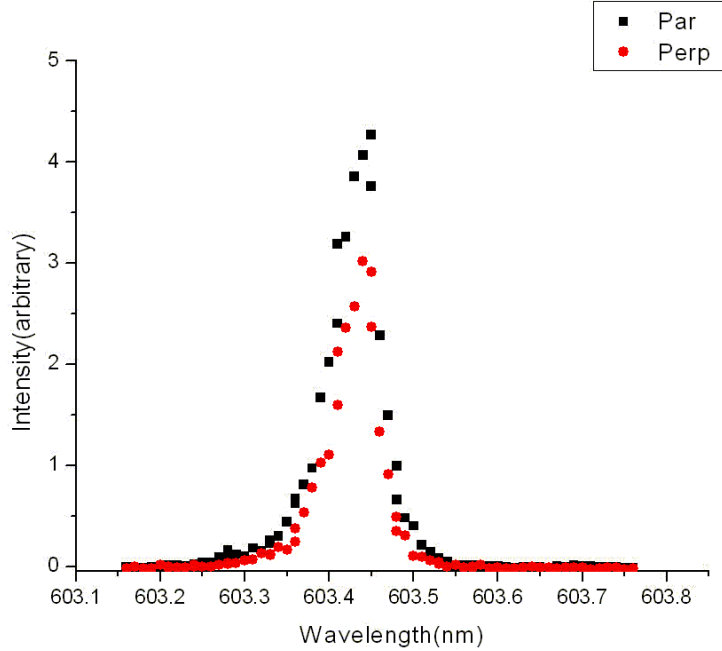


Figure 5.2: Polarization spectrum of the  $6s^2S_{1/2} \rightarrow 10s^2S_{1/2}$  transition.

Table 5.2: Calculated and measured polarization degrees.

	$P_{L_{calc}}$	$P_{L_{calc}}$ with hpf depolarization	$P_{L_{meas}}$ (this work)
$9d^2D_{5/2}$	60%	15.6%	15.76%(3)
$10s^2S_{1/2}$	14.28%	3.25%	3.7%(1.3)

## 5.4 Systematic Effects

In this section we will discuss about the systematic effects on the polarization spectrum and how we can minimize this effects in order to improve the accuracy of our measurements.

Imperfections of the polarizers and the birefringence in the windows of the oven and cell may slightly change the polarization direction, the collinearity and the uniformity of the laser beams, which in turn will affect the measured polarization degree. Thus, we check these effects using polarizers before and after the lasers entering the cell. The polarization of the two laser beams were accomplished with the use of two Glan-Thompson polarizers. The extinction ratio of the polarizers were checked to purify the polarization of the lasers. Linearity, uniformity and alignment of the laser beams were checked daily by sending them with a use of mirrors to a few meters away from the oven. This method ensures that the laser beams are aligned and overlap well.

Other factors that may change the degree of polarization are temperature and

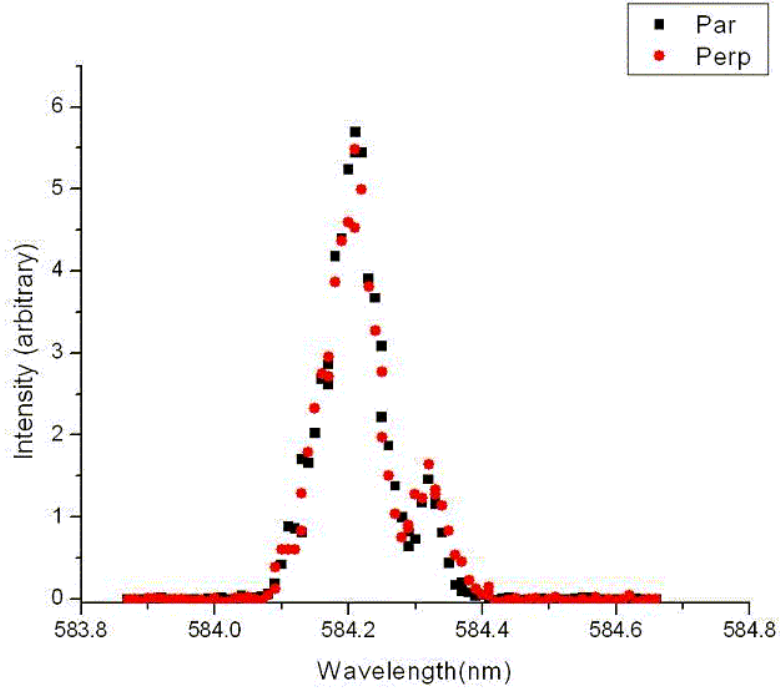


Figure 5.3: Polarization spectrum of the  $6s^2S_{1/2} \rightarrow 9d^2D_{5/2}$  transition.

the powers of the lasers. The results of our measurements on these effects are explained in the following sub-sections. The temperature effect may cause radiation trapping which occurs in very dense media where the radiation of the excited state is trapped inside the cell and bounces back and forth between the absorbers. This may cause a decrease in the polarization degree. Radiation trapping lengthens the lifetime of the excited state and shortens the decay rate of the atoms. Since our laser pulse is short compared to the lifetime of the excited state, radiation trapping may not be considered to be an effect.

In gaseous media the doppler effect may play an important role of broadening the spectral lines. Doppler broadening is caused due to different velocities of the atoms and their thermal distribution and can be written according to the Boltzmann distribution. Due to the different frequency positions in the gain curve, the excited atoms cannot change their excitation energies with each other and the lasing of several axial modes leads to a drop of population inversion which can be observed as narrow dips in the doppler gain profile. If the medium is excited by a laser beam at a certain frequency  $w'$  only certain group of atoms can make the real transition. The thermal velocity of this group should satisfy the relation  $kv' = w' - w_0$ , where  $k$  is the wave vector of the laser beam and  $w_0$  is the central frequency of the Doppler line [24]. In other words, those atoms at exact resonance with the laser frequency do not simply absorb the field and find themselves excited into their upper level. They are ready to emit instead of absorb. Whereas the atoms on off-resonance frequency behave as normal absorbers. This effect usually

occurs when the field is weak and causes to narrow dips in the doppler-broadened gaussian line profile which is known as the “hole burning” effect. In our experiment we did not observe hole burning effect [25–27].

### 5.4.1 Temperature Effect

We varied the temperature of the Cs cell in order to check the density dependence of the polarization. The temperature of the cell was varied from  $60^{\circ}\text{C}$  to  $120^{\circ}\text{C}$  for the  $6s^2S_{1/2} \rightarrow 6p^2P_{3/2} \rightarrow 10s^2S_{1/2}, 9d^2D_{5/2}$  transitions. The result of the polarization measurements in changing densities showed within the statistical errors that the linear polarization spectrum was independent of the temperature factor. The results are shown in Fig. 5.4 and 5.5.

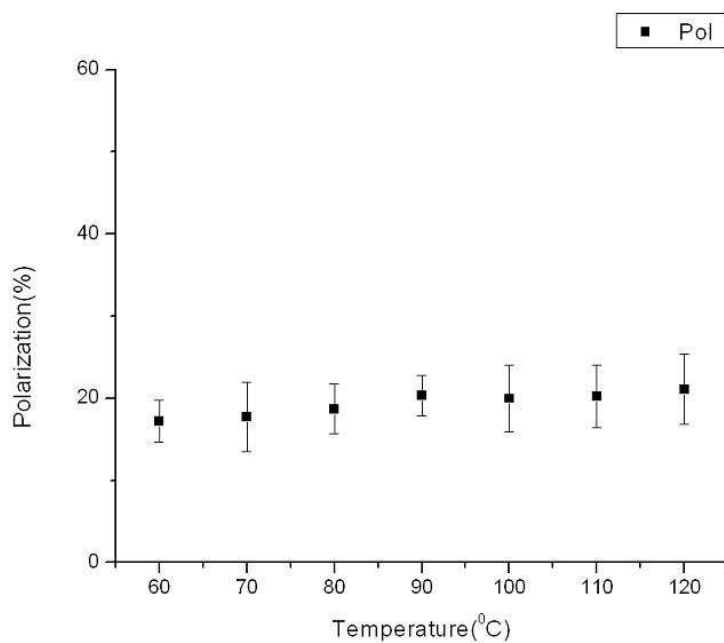


Figure 5.4: Polarization degree at various temperatures of Cs for the 6S-10S state excitation.

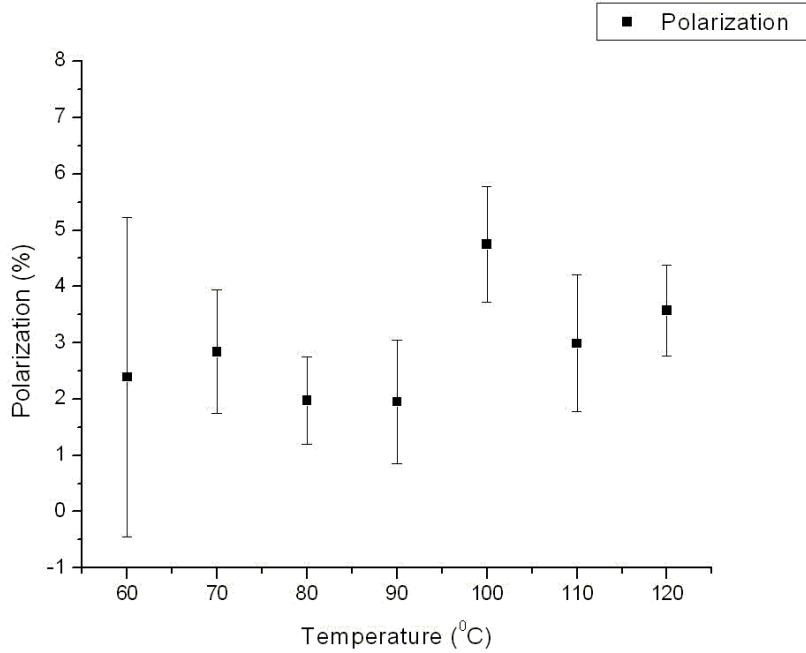


Figure 5.5: Polarization degree at various temperatures of Cs for the 6S-9D state excitation.

### 5.4.2 Laser Power Effect

The laser power dependence of the two-photon  $6s^2S_{1/2} \rightarrow 6p^2P_{3/2} \rightarrow 9d^2D_{5/2}$  transition were checked. We attenuated the lasers individually to see if there was any effect of the dye laser powers in the polarization spectrum. The power of laser 1 was reduced by a factor of 10 and that of laser 2 was reduced by a factor of 4. The power dependence data of the lasers is taken at 70°C. The graphs for the polarization versus power of the lasers are shown in Fig. 5.6 and 5.7. Our measurement shows that within the statistical errors there was no power dependence in the polarization spectrum. Also, the power dependence maybe done to check if there was a hole burning effect in the polarization spectrum. In this case, one may expect to see a higher polarization degree.

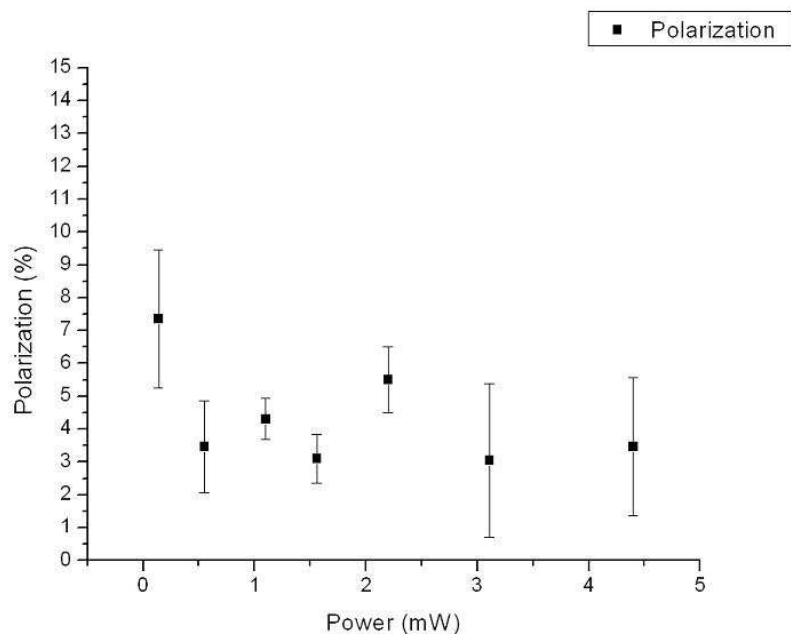


Figure 5.6: Power dependence of laser 1 on the polarization spectrum for the  $9d^2D_{5/2}$  state.

### 5.4.3 Depolarization with Argon Buffer Gas

We obtained the linear polarization spectrum of Cs in the presence of Ar buffer gas in the  $6s^2S_{1/2} \rightarrow 10s^2S_{1/2}, 9d^2D_{5/2}$  transitions. The degree of polarization has a strong pressure dependence when collisions between the excited states Cs and ground state Ar atoms take place. Our polarization data shows strong collisional depolarization due to the effect of argon collisions with the cesium atom. Fig 5.8 shows the polarization degree with various pressure of argon buffer gas. The circle black data points in Fig 5.8 refer to the polarization degree of the  $6s^2S_{1/2} \rightarrow 10s^2S_{1/2}$  transition and the square red data points refer to that of the  $6s^2S_{1/2} \rightarrow 10d^2D_{1/2}$  transition. The pressure and the polarization degree data with the statistical errors for the  $10s^2S_{1/2} \rightarrow 6s^2S_{1/2}$  transition and the  $9d^2D_{5/2} \rightarrow 6s^2S_{1/2}$  transition are listed in Table 5.3 and 5.4.

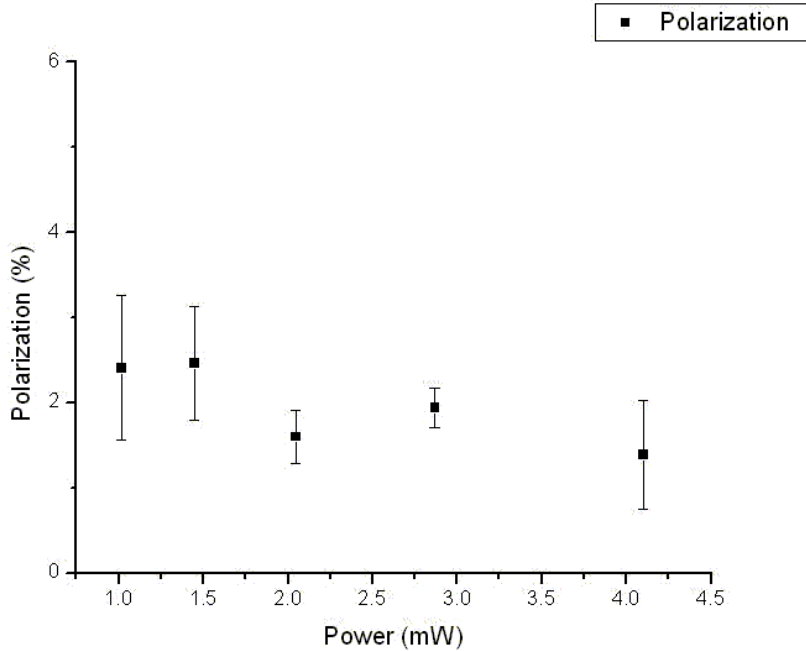


Figure 5.7: Power dependence of laser 2 on the polarization spectrum for the  $9d^2 D_{5/2}$  state.

#### 5.4.4 Extracting the Depolarization Cross Section

In this section, we show briefly the derivation of the polarization in terms of the collisional depolarization cross section ( $\sigma_d$ ) using rate equation analysis. After finding the polarization in terms of pressure and  $\sigma_d$ , we applied a weighted non-linear least-square fit to obtain the best value of  $\sigma_d$ .

We investigated the collisional depolarization of the two-photon  $6s^2 S_{1/2} \rightarrow 6p^2 P_{3/2} \rightarrow 10s^2 S_{1/2}, 9d^2 D_{5/2}$  atomic transitions of Cs with different Ar buffer gas pressures ranging from 5 Torr to 100 Torr. In this section we show how to extract the collisional cross section of the  $6p^2 P_{3/2}$  intermediate state from the measured linear polarization spectrum. Fig 5.8 shows the polarization measurement versus pressure for the  $6s^2 S_{1/2} \rightarrow 10s^2 S_{1/2}, 9d^2 D_{5/2}$  transitions.

We can write the atomic transitions from  $6s^2 S_{1/2}$  state to the  $9d^2 D_{5/2}$  state in terms of the rate equation and alignment. Hence, the collisional depolarization of the polarization spectrum occurs in the  $6p^2 P_{3/2}$  state, it is sufficient to do the calculations for the  $6s^2 S_{1/2} \rightarrow 6p^2 P_{3/2} \rightarrow 10s^2 S_{1/2}$  transition.

The time dependent total population density in terms of pump pulse rate can be written as

$$N(t) = \frac{2\Gamma_P}{\gamma}(1 - e^{-\gamma t}) \quad (5.1)$$

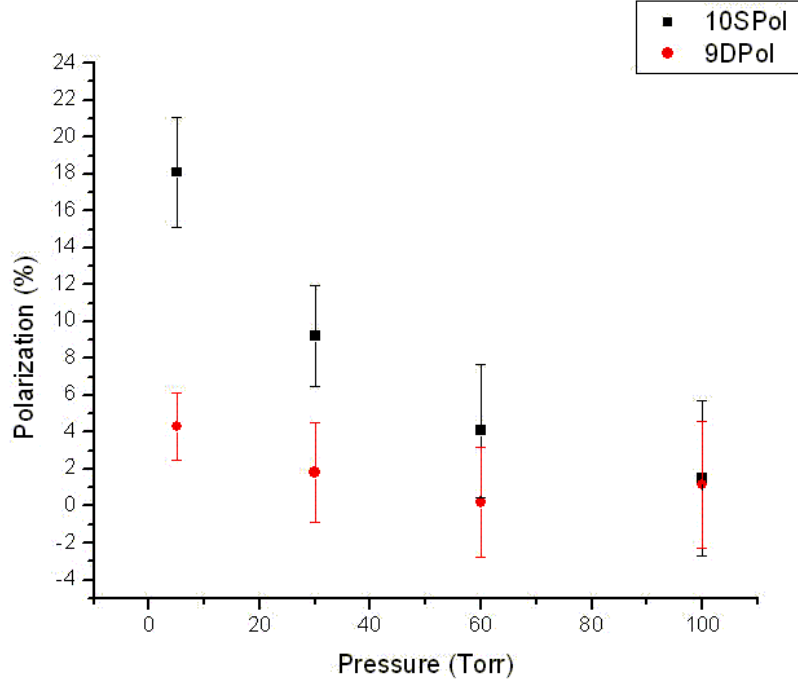


Figure 5.8: Depolarization of the  $6s^2S_{1/2} \rightarrow 10s^2S_{1/2}, 9d^2D_{5/2}$  transition in the presence of different argon buffer gas pressures.

and the alignment as

$$\langle A_0(t) \rangle = -\frac{8}{5} \frac{\Gamma_P}{\gamma_T} (1 - e^{-\gamma_T t}). \quad (5.2)$$

The population density for the  $m = \frac{1}{2}$  quantum state is

$$N_{1/2}(t) = \frac{N(t) - \frac{10}{8} \langle A_0(t) \rangle g^{(2)}}{4} \quad (5.3)$$

and for the  $m = \frac{3}{2}$  quantum state we can write the population density as

$$N_{3/2}(t) = \frac{N(t) + \frac{10}{8} \langle A_0(t) \rangle g^{(2)}}{4}. \quad (5.4)$$

By substituting Eq. 5.1 and 5.2 into Eq. 5.3 and 5.3 we will find the population densities in the  $m = \frac{1}{2}$  and  $m = \frac{3}{2}$  quantum states in terms of decay rates as

$$N_{1/2}(t) = \frac{\Gamma_P}{2} \left[ \frac{1}{\gamma} (1 - e^{-\gamma_T t}) + \frac{1}{\gamma_T} (1 - e^{-\gamma t}) \right] \quad (5.5)$$

$$N_{3/2}(t) = \frac{\Gamma_P}{2} \left[ \frac{1}{\gamma} (1 - e^{-\gamma_T t}) - \frac{1}{\gamma_T} (1 - e^{-\gamma t}) \right]. \quad (5.6)$$

Table 5.3: Our work on the depolarization with argon buffer gas in the  $6s^2S_{1/2} \rightarrow 10s^2S_{1/2}$  transition.

<i>Argon Pressure(Torr)</i>	<i>Polarization of <math>10s^2S_{1/2}</math>(%)</i>	<i>Error(%)</i>
<i>pure Cs</i>	15.76	(3)
5	18.1	(3.01)
30	9.2	(2.75)
60	4.08	(3.61)
100	1.51	(4.2)

Table 5.4: Depolarization with argon buffer gas in the  $6s^2S_{1/2} \rightarrow 9d^2D_{5/2}$  transition.

<i>Argon Pressure(Torr)</i>	<i>Polarization of <math>9d^2D_{5/2}</math>(%)</i>	<i>Error(%)</i>
<i>pure Cs</i>	3.7	(1.3)
5	4.31	(1.82)
30	1.8	(2.7)
60	-0.22	(2.96)
100	1.15	(3.46)

For simplicity we can call  $\frac{1}{\gamma}(1 - e^{-\gamma t}) = P_1$  and  $\frac{1}{\gamma T}(1 - e^{-\gamma T t}) = P_2$  and since  $\Gamma_P$  will cancel out at the end we neglect this term. The population in the  $m = \frac{1}{2}, \frac{3}{2}$  quantum states can than be written as,

$$N_{1/2}(t) = \frac{1}{2}(P_1 + P_2) \quad (5.7)$$

$$N_{3/2}(t) = \frac{1}{2}(P_1 - P_2) \quad (5.8)$$

The parallel signal for  $\Delta m = 0$  transition from the  $m = \frac{1}{2}$  quantum state is

$$S_{\parallel} = \frac{1}{3} \int_0^T N_{1/2}(t) dt \quad (5.9)$$

by substituting Eq. 5.7 into 5.9 we will obtain

$$S_{\parallel} = \frac{1}{6} \int_0^T P_1 + \frac{1}{6} \int_0^T P_2 \quad (5.10)$$

The perpendicular signal can be found for  $\Delta m = \pm 1$  transitions from the  $m = \frac{1}{2}$  and  $m = \frac{3}{2}$  quantum states as

$$S_{\perp} = \frac{1}{4} \int_0^T N_{3/2}(t) dt + \frac{1}{12} \int_0^T N_{1/2}(t) dt \quad (5.11)$$

Finally if we substitute Eq. 5.7 and 5.8 into 5.11 the perpendicular signal can be written as

$$S_{\perp} = \frac{1}{6} \int_0^T P_1 - \frac{1}{12} \int_0^T P_2 \quad (5.12)$$

The linear polarization can be found with the following equation

$$P_L = \frac{S_{\parallel} - S_{\perp}}{S_{\parallel} + S_{\perp}} \quad (5.13)$$

where

$$S_{\parallel} - S_{\perp} = \frac{1}{4} \int_0^T P_2 \quad (5.14)$$

and

$$S_{\parallel} + S_{\perp} = \frac{1}{3} \int_0^T P_1 + \frac{1}{12} \int_0^T P_2 \quad (5.15)$$

Using the equation given above the linear polarization can be written as

$$P_L = \frac{3 Z}{4 + Z} \quad (5.16)$$

where

$$Z = \frac{g^{(2)}\gamma}{\gamma T} \frac{\left[1 - \frac{1}{\gamma T}(1 - e^{-\gamma T})\right]}{\left[1 - \frac{1}{\gamma T}(1 - e^{-\gamma T})\right]} \quad (5.17)$$

$\gamma$  is the radiative decay rate of the  $6p^2P_{3/2}$  intermediate state and can be calculated from the life time of the state

$$\gamma = \frac{1}{\tau_{6P_{3/2}}} \quad (5.18)$$

$T$  is the temporal pulse width of the laser and  $g^{(2)}$  is the hyperfine depolarization coefficient.

The other undefined quantity is

$$\gamma_T = \gamma + \Gamma \quad (5.19)$$

where

$$\begin{aligned} \Gamma &= \rho_{Ar} \sigma_d \bar{v}_{Ar-Cs} \\ &= \rho_{Ar} k_d \\ &= \frac{P}{kT} \cdot k_d \end{aligned} \quad (5.20)$$

In the above equation  $k_d$  is the disalignment rate coefficient,  $\sigma_d$  is the collisional depolarization cross section and  $\bar{v}_{Ar-Cs}$  is the average velocity of the Cs-Ar atoms and can be found from the equation

$$\bar{v} = \sqrt{\frac{8kT}{\pi\mu}} \quad (5.21)$$

Table 5.5: Constants used in Eq.5.16 to extract collisional depolarization cross section from the polarization spectrum (\* [1]).

$\tau_{P_{3/2}}$	30.67ns
$m_{Ar}$	$6.634 \times 10^{-26} kg$
$m_{Cs}$	$2.206 \times 10^{-25} kg$
$\mu_{Ar-Cs}$	$5.1 \times 10^{-26} kg$
$\gamma_{6P_{3/2}}$	$3.26 \times 10^7 s^{-1}$
$\bar{v}_{Ar-Cs}$	486.38 m/s
1 Torr	$133.32 Nm^{-2}$
$T_{pulse}$	$6 \times 10^{-9} s$
$k_{Boltzmann}$	$1.3807 \times 10^{-23} JK^{-1}$
$T(\text{temperature})$	$343.15 K^0$
$R$	$8.3145 Jmol^{-1} K^{-1}$
$*g^{(2)}$	0.219
$h^{(2)}(\frac{3}{2}, \frac{1}{2})$	-1.25
$h^{(2)}(\frac{3}{2}, \frac{5}{2})$	-0.25
$\langle A_0 \rangle$	-0.8

where  $k$  is the boltzmann constant,  $T$  is the temperature of the cesium cell and  $\mu$  is the reduced mass of the Cs-Ar atoms.

Substituting Eq. 5.20 into Eq. 5.19 then Eq. 5.20 into Eq. 5.16, we can extract the collisional depolarization cross section by using a weighted non-linear least-square fit as shown in Fig. 5.4.4. In the Eq. 5.16,  $P_L$  is the measured polarization,  $P$  is the pressure and  $\sigma_d$  is the only fitting parameter. The numerical values used to extract the  $\sigma_d$  is shown in Table 5.5. Our measured  $\sigma_d$  and the reported values [9, 12] are shown in Table 5.6.

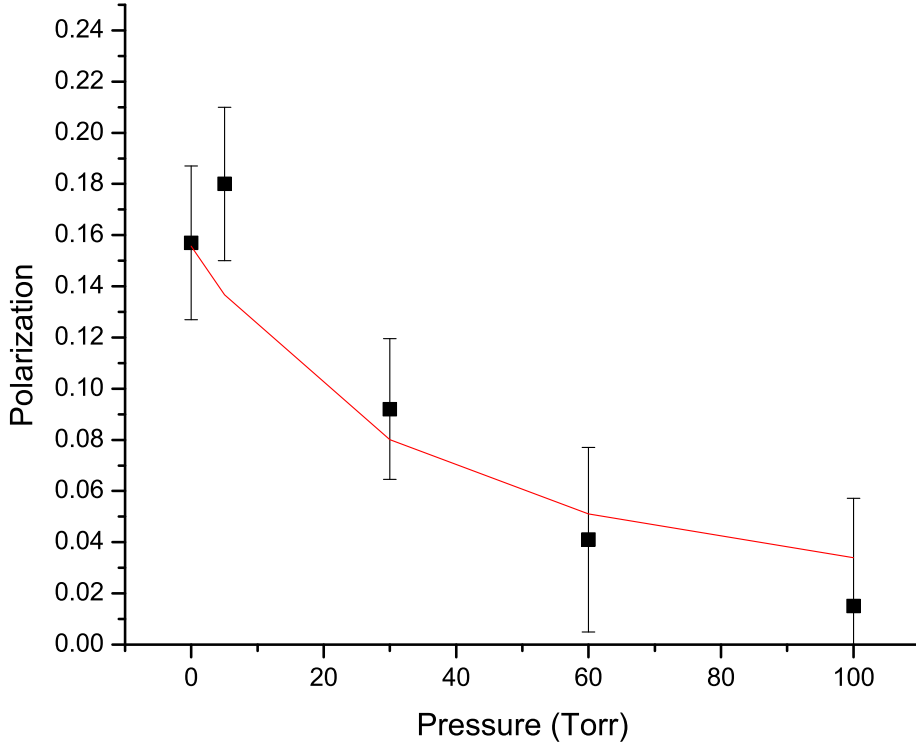


Figure 5.9: Weighted non-linear least square fit of the polarization spectrum of Cs in the vicinity of Ar atoms.

Table 5.6: Collisionaldepolarization cross sections of the  $6p^2P_{3/2}$  Cs atom

$\sigma_d$ ( $\text{\AA}^2$ )	
159( $\pm 58$ )	this work
225( $\pm 35$ )	Guiry(exp.) [9]
212	Rebane and Rebane(theo.) [13]

The goal of weighted non-linear least-square fit is to find the best values using nonlinear regression for the parameter  $\sigma_d$  of the Eq. 5.16.

This method generate a curve that minimizes the sum of the squares of the vertical distance between the data points and curve. If the scatter is uniform, least-squares regression minimizes

$$\sum (Y_{data} - Y_{curve})^2 \quad (5.22)$$

and finds the parameter value that is most likely to be correct.

If the average amount of data is not uniform (increases/decreases as  $Y$  increases/decreases), a least-squares method tends to give undue to the points with

large  $Y$ -values, and ignores points with low  $Y$ -values. In order to prevent this, it is common to apply a weighting scheme. Thus, the best alternate to minimizing the sum of the squares of the vertical distances of the points from the curve is to minimize the sum of the squares of the relative distances of the points from the curve. That is called relative weighting and is

$$\sum \left( \frac{Y_{data} - Y_{curve}}{Y_{data}} \right)^2 \quad (5.23)$$

## 5.5 Conclusion

An experimental study of linear polarization spectrum in atomic  $^{133}\text{Cs}$  for the  $6s^2S_{1/2} \rightarrow 10s^2S_{1/2}, 9d^2D_{5/2}$  atomic on resonance transitions have been made by using a two-photon two-color excitation process. We investigated a collisional depolarization spectrum of the  $6s^2S_{1/2} \rightarrow 6p^2P_{3/2} \rightarrow 10s^2S_{1/2}, 9d^2D_{5/2}$  transitions with Ar buffer gas. A pump-probe technique was used to observe a doppler free polarization spectrum and to minimize systematic effects such as radiation trapping and line broadening. In the present study a hyperfine depolarization effect in the  $6p^2P_{3/2}$  intermediate state was observed. Our linear polarization degree measurements in the absence of argon buffer gas are in excellent agreement with the theoretical and experimental values found in [1] due to the dependence of the  $g^{(2)}$  hyperfine depolarization coefficient. In the presence of argon buffer gas, the polarization spectrum of cesium shows a pressure dependence, hence a strong depolarization due to the collisions between the excited state Cs and the ground state Ar gas, as shown in 5.8. The depolarization of cesium was obtained in relation to different argon buffer gas pressures varying from 5 Torr to 100 Torr. A collisional depolarization cross section was then extracted from the measured polarization spectrum. The collisional depolarization cross section we found in the  $6p^2P_{3/2}$  state is in satisfactory agreement with [9].

Future experiment with the two-photon two-color approach would be to study the disorientation cross section in the  $6p^2P_{1/2}$  state using circularly polarized light, effect of different buffer gases on the depolarization spectrum, the effects of magnetic field on the polarization spectrum, and the quantum beat spectroscopy to investigate the hyperfine levels in the highly excited states of Cs.

# Bibliography

- [1] M.D. Havey and L.L. Vahala. Comment on orientation, alignment and hyperfine effects on dissociation of diatomic molecules to open shell atoms. *J.Chem.Phys*, 86:1648, 1987.
- [2] Yuri Rostovtsev Olga Kocharovskaya and Marlan O. Scully. Stopping light via hot atoms. *Physical Review Letters*, 86:628, 2001.
- [3] A. G. Litvak and M. D. Tokman. Electromagnetically induced transparency in ensembles of classical oscillators. *Physical Review Letters*, 88:095003, 2002.
- [4] Sune Svan. *Atomic and Molecular Spectroscopy*. Springer Verlag, Berlin Heidelberg, 1992.
- [5] M. Inguscio E. Arimondo and P. Violino. Experimental determinations of the hyperfine structure in the alkali atoms. *Reviews of Modern Physics*, 49:31, 1977.
- [6] Harold J. Metcalf and Peter van der Straten. *Laser Cooling and Trapping*. Springer, New York, 1999.
- [7] Helmut W. Hellwig. Atomic frequency standarts: A survey. *Proceedings of the IEEE*, 63:212, 1975.
- [8] J. Haas J. Fricke and E. Lüscher. Cross sections for excited-state mixing in cesium-noble gas collisions from  $d_2$  optical pumping. *Physical Review*, 163:45, 1967.
- [9] J. Guiry and L. Krause. Depolarization of  $6p_{3/2}$  cesium atoms, induced in collisions with noble gases. *Physical Review A*, 14:2034, 1976.
- [10] M. Havey L. Cook, D. Olsgaard and A. Sierazdan. Collisional modification of the atomic na  $3s^2s_{1/2} - 5s^2s_{1/2}$  two-color two-photon polarization spectrum. *Physical Review A*, 47:340, 1993.
- [11] Allan Gallagher. Collisional depolarization of the rb 5p and cs 6p doublets. *Physical Review*, 157:68, 1967.
- [12] A. I. Okunevich and V. I. Perel. Relaxation in the sublevel system of the excited state of alkali metal atoms colliding with noble gas atoms. *Soviet Physics JETP*, 31:356, 1970.

- [13] T. K. Rebane V. N. Rebane and V.A. Cherenkovski. Impact depolarization of atoms in the presence of hyperfine structure. *Opt. Spectrosc.*, 33:337, 1972.
- [14] Raymond Chang. *Basic Principles of Spectroscopy*. McGraw-Hill Kogakusha,Ltd., Japan, 1971.
- [15] Rodney Loudon. *The Quantum Theory of Light*. Oxford University Press, New York, 1983.
- [16] M.E.Rose. *Elementary Theory of Angular Momentum*. John Wiley and Sons,Inc., New York, 1957.
- [17] Richard L. Liboff. *Intorductory Quantum Mechanics*. Holden-Day, Inc., San Fransisco, 1999.
- [18] Eugen Merzbacher. *Quantum Mechanics*. John Wiley and Sons, New York, 1970.
- [19] U. Fano and Joseph H. Macek. Impact excitation and polarization of the emitted light. *Rev. Mod. Phys.*, 45:553, 1973.
- [20] Chris H. Greene and Richard N. Zare. Photofragment alignment and orientation. *Ann. Rev. Phys. Chem.*, 33:119, 1982.
- [21] S.Bashkin. *Topics in Current Physics: Beam-Foil Spectroscopy*. Springer-Verlag, New York, 1976.
- [22] H.J.Andrä. Fine structure, hyperfine structure and lamb shift measurements by the beam-foil technique. *Physica Scripta*, 9:257, 1974.
- [23] F. J. Duarte. *Dye Laser Principles: With Applications*. Academic Press, Inc., New York, 1990.
- [24] Song H. Liu Guang S. He. *Physics of Nonlinear Optics*. World Scientific Publishing Co., New Jersey, 1999.
- [25] W. Demtröder. *Laser Spectroscopy*. Springer-Verlag, New York, 1996.
- [26] L. Allen and J.H. Eberly. *Optical Resonance and Two-Level Atoms*. John Wiley and Sons, Inc., New York, 1975.
- [27] Hanle and Kleinoppen. *Progress in Atomic Spectroscopy Part B*. Plenum Press, New York, 1978.
- [28] A. A. Radzig and B. M. Smirnov. *Reference Data on Atoms, Molecules and Ions*. Springer-Verlag, New York, 1985.

# Appendix A

## Density Matrix Elements

The polarization degree of the  $6s^2S_{1/2} \rightarrow 10s^2S_{1/2}, 9d^2D_{5/2}$  can also be calculated by using density matrix elements.

Each excitation on the energy levels can be written in density matrix elements and than be combined to calculate the intensities for  $\Delta m = 0$  and  $\Delta m = \pm 1$ , when both of the lasers are parallel and perpendicular to each other, respectively. The intensities for each case is the sum of the square of the density matrices. The polarization degree can than be calculated from Eq. (refer to equation).

The general form of the the density matrix elements is given as

$$\langle j'm' | T_q^k | jm \rangle = C(jk j'; m q m') \langle j' || T^k || j \rangle \quad (\text{A.1})$$

where  $\langle j' || T^k || j \rangle$  is the reduced matrix elements of the tensor operator  $T_q^k$  and it is independent of the  $m_1, m_2$  quantum numbers. The notation  $j'm'$  refers to the quantum numbers in the final and  $jm$  to the initial state.  $k$  refers to the rank of the tensor operator and  $q$  is the total quantum number of the transition. The first term on the RHS is called as the Clebsch-Gordan coefficient or C-coefficient and it contains the conservation of the angular momentum, therefore vanishes unless  $m' = q + m$ . However the tables for the C-coefficients are given in a different notation, where  $j' = j_2, j = j_1, m' = m_2, m = m_1, k = j$  and  $q = m$ . We present the polarization degree calculation for the  $6s^2S_{1/2} \rightarrow 10s^2S_{1/2}$  transition.

The density matrix for the first transition from the initial to the intermediate state which is labeled in Fig. A.1 as A can be written as

$$\begin{aligned} \langle j_2 m_2 | r_q | j_1 m_1 \rangle &= \left\langle \frac{3}{2} - \frac{1}{2} \left| r_0 \right| \frac{1}{2} - \frac{1}{2} \right\rangle \\ &= C\left(\frac{1}{2} \frac{3}{2} 1; -\frac{1}{2} - \frac{1}{2} 0\right) \left\langle \frac{3}{2} || T^k || \frac{1}{2} \right\rangle \end{aligned} \quad (\text{A.2})$$

where  $r_q$  is the position vector in spherical coordinates and is given as

$$\begin{aligned} \hat{r}_x &= (r_{-1} - r_{+1})/\sqrt{2} \\ \hat{r}_y &= i(r_{-1} + r_{+1})/\sqrt{2} \end{aligned}$$

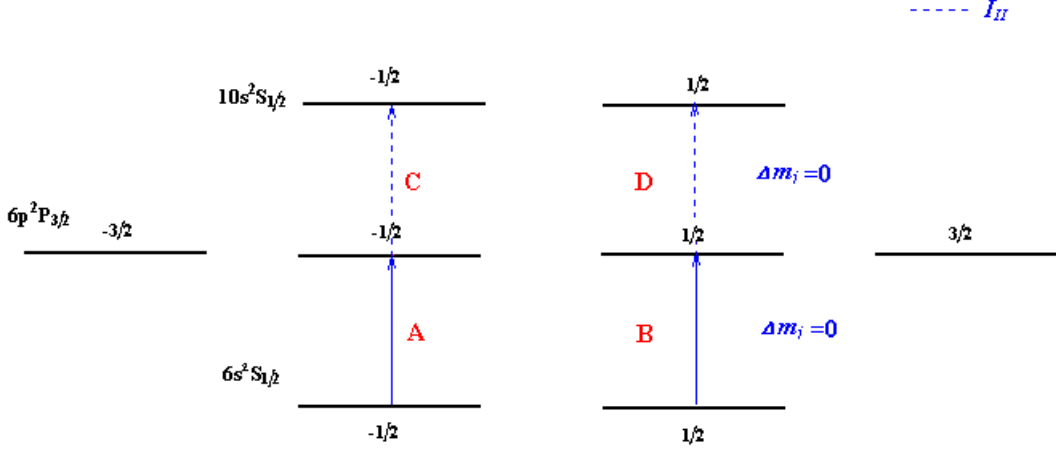


Figure A.1: Kastler diagram of the levels for  $I_{||}$ .

$$\hat{r}_z = r_0 \tag{A.3}$$

For the second transition labeled with B

$$\left\langle \frac{3}{2} \frac{1}{2} \mid r_0 \mid \frac{1}{2} \frac{1}{2} \right\rangle = C\left(\frac{1}{2} \frac{3}{2} 1; \frac{1}{2} \frac{1}{2} 0\right) \left\langle \frac{3}{2} \parallel T^k \parallel \frac{1}{2} \right\rangle \tag{A.4}$$

The density matrix from the intermediate to the final state for the transition which is labeled as C

$$\left\langle \frac{1}{2} -\frac{1}{2} \mid r_0 \mid \frac{3}{2} -\frac{1}{2} \right\rangle = C\left(\frac{3}{2} \frac{1}{2} 1; -\frac{1}{2} -\frac{1}{2} 0\right) \left\langle \frac{1}{2} \parallel T^k \parallel \frac{3}{2} \right\rangle \tag{A.5}$$

Finally for D

$$\left\langle \frac{1}{2} \frac{1}{2} \mid r_0 \mid \frac{3}{2} \frac{1}{2} \right\rangle = C\left(\frac{3}{2} \frac{1}{2} 1; \frac{1}{2} \frac{1}{2} 0\right) \left\langle \frac{1}{2} \parallel T^k \parallel \frac{3}{2} \right\rangle \tag{A.6}$$

The C-coefficients for the matrices above with  $j_2 = \frac{1}{2}$  are calculated and given in Table A.1.

The Clebsch-Gordan coefficient table gives us equations to calculate the desired transition. The equation changes for each state and quantum numbers. We included only the coefficient equations for the transition we are interested, more details can be found in [16] and [28]

Table A.1:  $(j_1 \frac{1}{2} m_1 m_2 | j_1 \frac{1}{2} j m)$

$j =$	$m_2 = \frac{1}{2}$	$m_2 = -\frac{1}{2}$
$j_1 - \frac{1}{2}$	$-\sqrt{\frac{j_1 - m + \frac{1}{2}}{2j_1 + 1}}$	$\sqrt{\frac{j_1 + m + \frac{1}{2}}{2j_1 + 1}}$

$$\left\langle \frac{3}{2} - \frac{1}{2} \mid r_0 \mid \frac{1}{2} - \frac{1}{2} \right\rangle = \sqrt{\frac{1}{2}} \left\langle \frac{3}{2} \parallel T^k \parallel \frac{1}{2} \right\rangle \quad (\text{A.7})$$

$$\left\langle \frac{3}{2} \frac{1}{2} \mid r_0 \mid \frac{1}{2} \frac{1}{2} \right\rangle = -\sqrt{\frac{1}{2}} \left\langle \frac{3}{2} \parallel T^k \parallel \frac{1}{2} \right\rangle \quad (\text{A.8})$$

$$\left\langle \frac{1}{2} - \frac{1}{2} \mid r_0 \mid \frac{3}{2} - \frac{1}{2} \right\rangle = -\sqrt{\frac{1}{2}} \left\langle \frac{3}{2} \parallel T^k \parallel \frac{1}{2} \right\rangle \quad (\text{A.9})$$

$$\left\langle \frac{1}{2} \frac{1}{2} \mid r_0 \mid \frac{3}{2} \frac{1}{2} \right\rangle = \sqrt{\frac{1}{2}} \left\langle \frac{3}{2} \parallel T^k \parallel \frac{1}{2} \right\rangle \quad (\text{A.10})$$

The intensity for the parallel polarization is the combination of of the density matrix elements given above.

$$\begin{aligned} I_{\parallel} &= \left| \left\langle \frac{3}{2} - \frac{1}{2} \mid r_0 \mid \frac{1}{2} - \frac{1}{2} \right\rangle \left\langle \frac{1}{2} - \frac{1}{2} \mid r_0 \mid \frac{3}{2} - \frac{1}{2} \right\rangle \right|^2 + \\ &\quad \left| \left\langle \frac{3}{2} \frac{1}{2} \mid r_0 \mid \frac{1}{2} \frac{1}{2} \right\rangle \left\langle \frac{1}{2} \frac{1}{2} \mid r_0 \mid \frac{3}{2} \frac{1}{2} \right\rangle \right|^2 \\ &= \left| C\left(\frac{1}{2} \frac{3}{2} \ 1; -\frac{1}{2} - \frac{1}{2} \ 0\right) \left\langle \frac{3}{2} \parallel T^k \parallel \frac{1}{2} \right\rangle C\left(\frac{3}{2} \frac{1}{2} \ 1; -\frac{1}{2} - \frac{1}{2} \ 0\right) \left\langle \frac{1}{2} \parallel T^k \parallel \frac{3}{2} \right\rangle \right|^2 \\ &\quad + \left| C\left(\frac{1}{2} \frac{3}{2} \ 1; \frac{1}{2} \frac{1}{2} \ 0\right) \left\langle \frac{3}{2} \parallel T^k \parallel \frac{1}{2} \right\rangle C\left(\frac{3}{2} \frac{1}{2} \ 1; \frac{1}{2} \frac{1}{2} \ 0\right) \left\langle \frac{1}{2} \parallel T^k \parallel \frac{3}{2} \right\rangle \right|^2 \\ &= \frac{1}{2} \left| \left\langle \frac{1}{2} \parallel T^k \parallel \frac{3}{2} \right\rangle \left\langle \frac{3}{2} \parallel T^k \parallel \frac{1}{2} \right\rangle \right|^2 \end{aligned} \quad (\text{A.11})$$

For the perpendicular case the transition from the initial state to the intermediate state is the same since we only change the polarization of the second laser which excites the atoms from the intermediate to the final state.

The density matrix for the transition where  $\Delta m = -1$  which is labeled in Fig. A.2 as F can be written as

$$\begin{aligned} \left\langle \frac{1}{2} - \frac{1}{2} \mid r_x \mid \frac{3}{2} \frac{1}{2} \right\rangle &= \left\langle \frac{1}{2} - \frac{1}{2} \mid \frac{1}{\sqrt{2}}(r_+ - r_-) \mid \frac{3}{2} \frac{1}{2} \right\rangle \left\langle \frac{1}{2} \parallel T^k \parallel \frac{3}{2} \right\rangle \\ &= \left\{ \frac{1}{\sqrt{2}} \left\langle \frac{1}{2} - \frac{1}{2} \mid r_+ \mid \frac{3}{2} \frac{1}{2} \right\rangle - \frac{1}{\sqrt{2}} \left\langle \frac{1}{2} - \frac{1}{2} \mid r_- \mid \frac{3}{2} \frac{1}{2} \right\rangle \right\} \end{aligned}$$

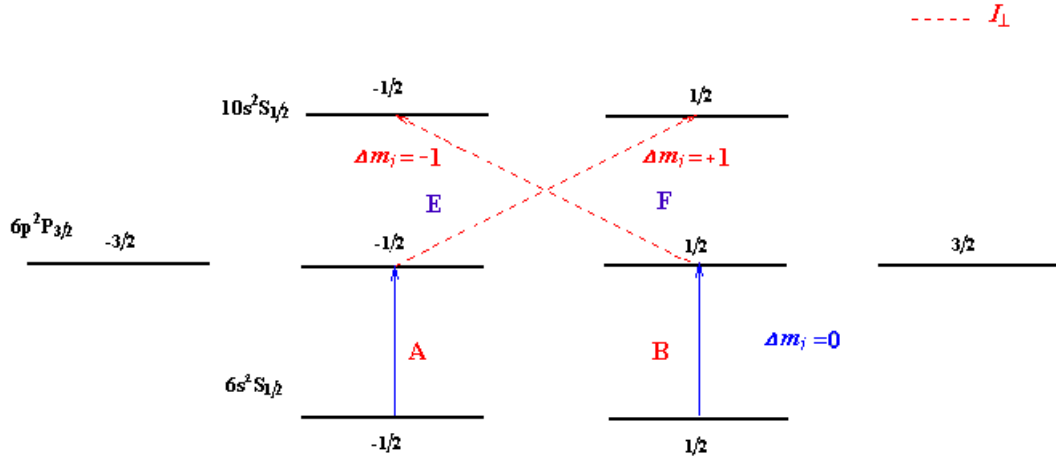


Figure A.2: Kastler diagram of the levels for  $I_{\perp}$ .

$$\begin{aligned}
 & \left\langle \frac{1}{2} \parallel T^k \parallel \frac{3}{2} \right\rangle \\
 = & \frac{1}{\sqrt{2}} \left\{ C\left(\frac{3}{2} \frac{1}{2} 1; \frac{1}{2} - \frac{1}{2} 1\right) - C\left(\frac{3}{2} \frac{1}{2} 1; \frac{1}{2} - \frac{1}{2} - 1\right) \right\} \\
 & \left\langle \frac{1}{2} \parallel T^k \parallel \frac{3}{2} \right\rangle
 \end{aligned} \tag{A.12}$$

The first C-coefficient in A.6 vanishes since the requirement for the conservation of angular momentum ( $m' = q + m$ ) is not fulfilled. This leaves us with

$$\left\langle \frac{1}{2} \quad -\frac{1}{2} \mid r_x \mid \frac{3}{2} \quad \frac{1}{2} \right\rangle = -\frac{1}{\sqrt{2}} C\left(\frac{3}{2} \frac{1}{2} 1; \frac{1}{2} - \frac{1}{2} - 1\right) \left\langle \frac{1}{2} \parallel T^k \parallel \frac{3}{2} \right\rangle \quad (\text{A.13})$$

The density matrix for the E transition where  $\Delta m = 1$

$$\begin{aligned} \left\langle \frac{1}{2} \quad \frac{1}{2} \mid r_x \mid \frac{3}{2} \quad -\frac{1}{2} \right\rangle &= \left\langle \frac{1}{2} \frac{1}{2} \mid \frac{1}{\sqrt{2}}(r_+ - r_-) \mid \frac{3}{2} - \frac{1}{2} \right\rangle \left\langle \frac{1}{2} \parallel T^k \parallel \frac{3}{2} \right\rangle \\ &= \left\{ \frac{1}{\sqrt{2}} \left\langle \frac{1}{2} \frac{1}{2} \mid r_+ \mid \frac{3}{2} - \frac{1}{2} \right\rangle - \frac{1}{\sqrt{2}} \left\langle \frac{1}{2} \frac{1}{2} \mid r_- \mid \frac{3}{2} - \frac{1}{2} \right\rangle \right\} \\ &\quad \left\langle \frac{1}{2} \parallel T^k \parallel \right\rangle \\ &= \frac{1}{\sqrt{2}} \left\{ C\left(\frac{3}{2} \frac{1}{2} 1; -\frac{1}{2} \frac{1}{2} 1\right) - C\left(\frac{3}{2} \frac{1}{2} 1; -\frac{1}{2} \frac{1}{2} - 1\right) \right\} \\ &\quad \left\langle \frac{1}{2} \parallel T^k \parallel \frac{3}{2} \right\rangle \end{aligned} \quad (\text{A.14})$$

Similar the second C-coefficient vanishes, therefore we can write the matrix element as

$$\left\langle \frac{1}{2} \quad \frac{1}{2} \mid r_x \mid \frac{3}{2} \quad -\frac{1}{2} \right\rangle = \frac{1}{\sqrt{2}} C\left(\frac{3}{2} \frac{1}{2} 1; -\frac{1}{2} \frac{1}{2} - 1\right) \left\langle \frac{1}{2} \parallel T^k \parallel \frac{3}{2} \right\rangle \quad (\text{A.15})$$

The C-coefficients for the matrices above for  $j_2 = \frac{3}{2}$  can be calculated from Table A.2 given below.

Table A.2:  $(j_1 \frac{3}{2} m_1 m_2 \mid j_1 \frac{3}{2} j m)$

$j =$	$m_2 = \frac{1}{2}$	$m_2 = -\frac{1}{2}$
$j_1 + \frac{1}{2}$	$-(j_1 - 3m + \frac{3}{2}) \sqrt{\frac{j_1 + m + \frac{1}{2}}{2j_1(2j_1 + 1)(2j_1 + 3)}}$	$(j_1 + 3m + \frac{3}{2}) \sqrt{\frac{j_1 - m + \frac{1}{2}}{2j_1(2j_1 + 1)(2j_1 + 3)}}$

$$\left\langle \frac{1}{2} \quad -\frac{1}{2} \mid r_x \mid \frac{3}{2} \quad \frac{1}{2} \right\rangle = \frac{1}{2} \left\langle \frac{1}{2} \parallel T^k \parallel \frac{3}{2} \right\rangle \quad (\text{A.16})$$

$$\left\langle \frac{1}{2} \quad \frac{1}{2} \mid r_x \mid \frac{3}{2} \quad -\frac{1}{2} \right\rangle = -\frac{1}{2} \left\langle \frac{1}{2} \parallel T^k \parallel \frac{3}{2} \right\rangle \quad (\text{A.17})$$

The intensity of the cascade fluorescence when the second laser is perpendicular to the first one can be written as

$$I_{\perp} = \left| \left\langle \frac{3}{2} \quad -\frac{1}{2} \mid r_0 \mid \frac{1}{2} \quad -\frac{1}{2} \right\rangle \left\langle \frac{1}{2} \quad -\frac{1}{2} \mid r_0 \mid \frac{3}{2} \quad \frac{1}{2} \right\rangle \right|^2 +$$

$$\begin{aligned}
& \left| \left\langle \frac{3}{2} \frac{1}{2} \mid r_0 \mid \frac{1}{2} \frac{1}{2} \right\rangle \left\langle \frac{1}{2} \frac{1}{2} \mid r_0 \mid \frac{3}{2} -\frac{1}{2} \right\rangle \right|^2 \\
&= \left| C\left(\frac{1}{2} \frac{3}{2} 1; -\frac{1}{2} -\frac{1}{2} 0\right) \left\langle \frac{3}{2} \parallel T^k \parallel \frac{1}{2} \right\rangle \left(-\frac{1}{\sqrt{2}}\right) C\left(\frac{3}{2} \frac{1}{2} 1; \frac{1}{2} -\frac{1}{2} -1\right) \left\langle \frac{1}{2} \parallel T^k \parallel \frac{3}{2} \right\rangle \right|^2 \\
&\quad + \left| C\left(\frac{1}{2} \frac{3}{2} 1; \frac{1}{2} \frac{1}{2} 0\right) \left\langle \frac{3}{2} \parallel T^k \parallel \frac{1}{2} \right\rangle \left(\frac{1}{\sqrt{2}}\right) C\left(\frac{3}{2} \frac{1}{2} 1; -\frac{1}{2} \frac{1}{2} -1\right) \left\langle \frac{1}{2} \parallel T^k \parallel \frac{3}{2} \right\rangle \right|^2 \\
&= \frac{1}{8} \left| \left\langle \frac{1}{2} \parallel T^k \parallel \frac{3}{2} \right\rangle \left\langle \frac{3}{2} \parallel T^k \parallel \frac{1}{2} \right\rangle \right|^2
\end{aligned} \tag{A.18}$$

The linear polarization degree can be found by substituting  $I_{\parallel}$  and  $I_{\perp}$  into Eq. 3.2 as  $P_L = 60\%$ .

The polarization degree for the  $6s^2S_{1/2} \rightarrow 9d^2D_{5/2}$  transition can be calculated in the same way by using the Clebsch-Gordan coefficients given in Table A.3. The calculated polarization degree was found as  $P_L = 14.28\%$ .

Table A.3: Clebsch-Gordan coefficients used in the experiment

$C\left(\frac{1}{2} \frac{3}{2} 1; \frac{1}{2} \frac{1}{2} 0\right)$	$-\sqrt{\frac{1}{2}}$
$C\left(\frac{3}{2} \frac{1}{2} 1; \frac{1}{2} \frac{1}{2} 0\right)$	$-\sqrt{\frac{1}{2}}$
$C\left(\frac{1}{2} \frac{3}{2} 1; -\frac{1}{2} -\frac{1}{2} 0\right)$	$\sqrt{\frac{1}{2}}$
$C\left(\frac{3}{2} \frac{1}{2} 1; -\frac{1}{2} -\frac{1}{2} 0\right)$	$\sqrt{\frac{1}{2}}$
$C\left(\frac{3}{2} \frac{1}{2} 1; \frac{1}{2} -\frac{1}{2} -1\right)$	$\frac{1}{2}$
$C\left(\frac{3}{2} \frac{1}{2} 1; -\frac{1}{2} \frac{1}{2} -1\right)$	$-\frac{1}{2}$
$C\left(\frac{3}{2} \frac{5}{2} 1; -\frac{1}{2} -\frac{1}{2} 0\right)$	$-\frac{1}{2}\sqrt{\frac{6}{5}}$
$C\left(\frac{3}{2} \frac{5}{2} 1; \frac{1}{2} \frac{1}{2} 0\right)$	$\frac{1}{2}\sqrt{\frac{6}{5}}$
$C\left(\frac{3}{2} \frac{5}{2} 1; -\frac{1}{2} -\frac{3}{2} 1\right)$	$\frac{1}{2}\sqrt{\frac{6}{5}}$
$C\left(\frac{3}{2} \frac{5}{2} 1; -\frac{1}{2} -\frac{3}{2} -1\right)$	$\frac{1}{2}\sqrt{\frac{1}{2}}$
$C\left(\frac{3}{2} \frac{5}{2} 1; -\frac{1}{2} \frac{1}{2} 1\right)$	$-\frac{1}{2}\sqrt{\frac{3}{5}}$
$C\left(\frac{3}{2} \frac{5}{2} 1; \frac{1}{2} -\frac{1}{2} 1\right)$	$-\frac{1}{2}\sqrt{\frac{3}{5}}$

# Appendix B

## LabVIEW Program

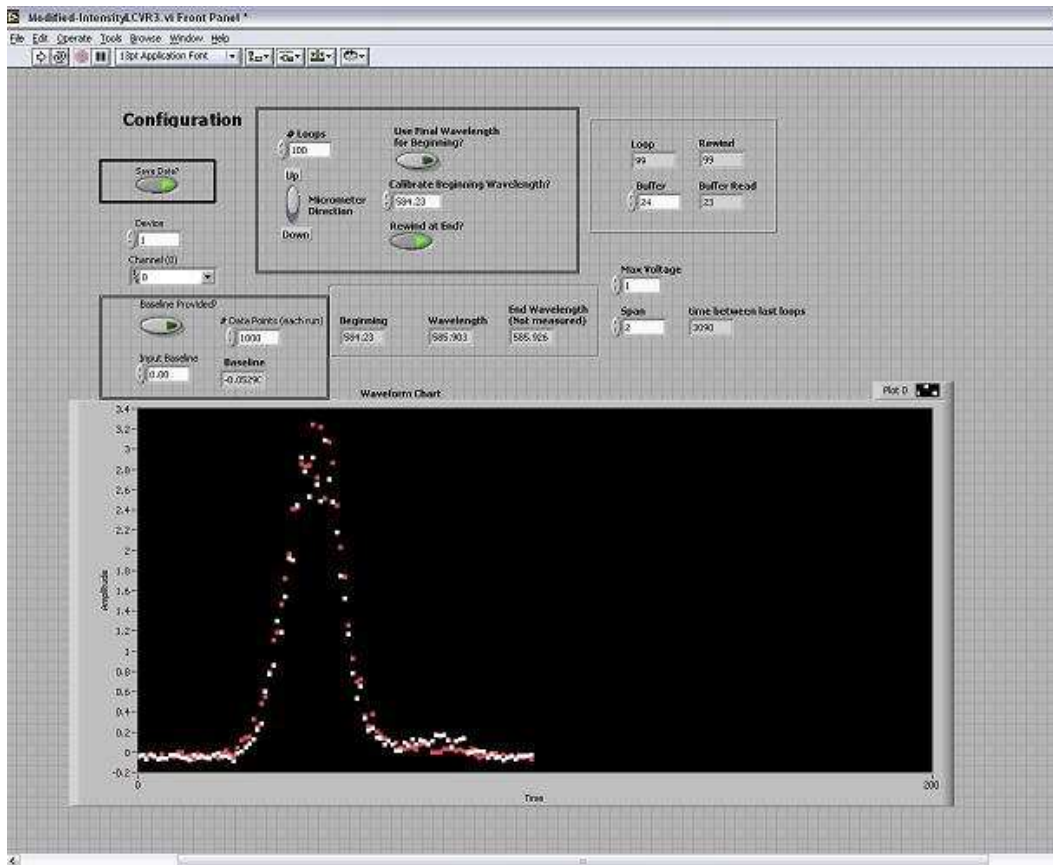


Figure B.1: Front panel of the LabVIEW control program.

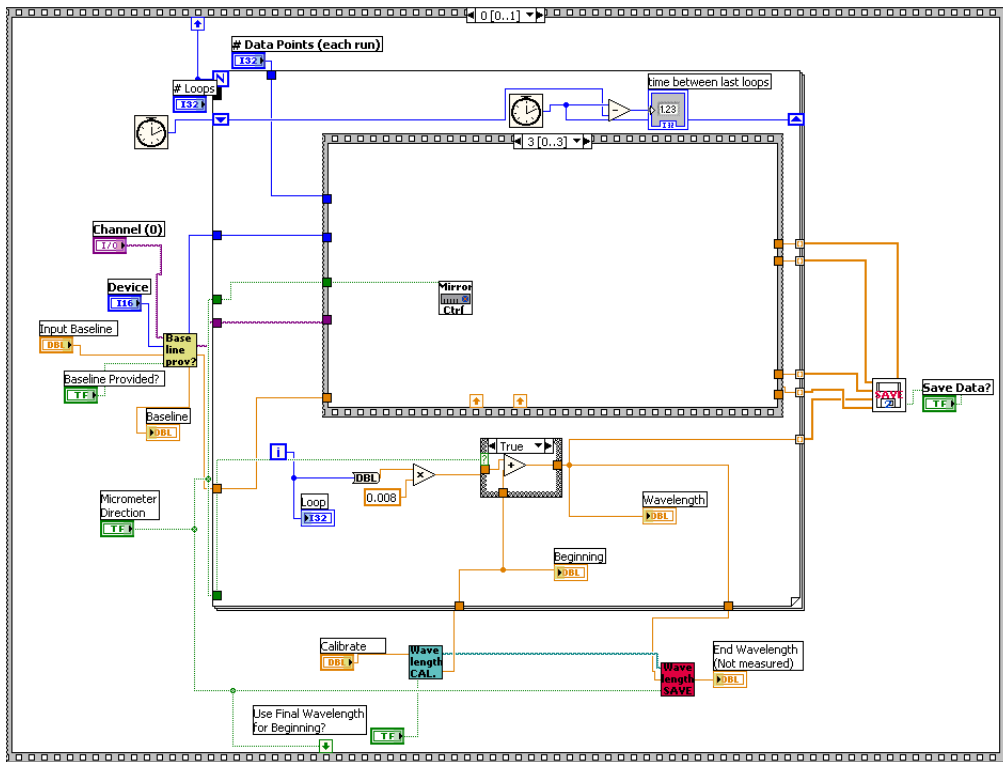


Figure B.2: Block diagram to control the stepper motor.

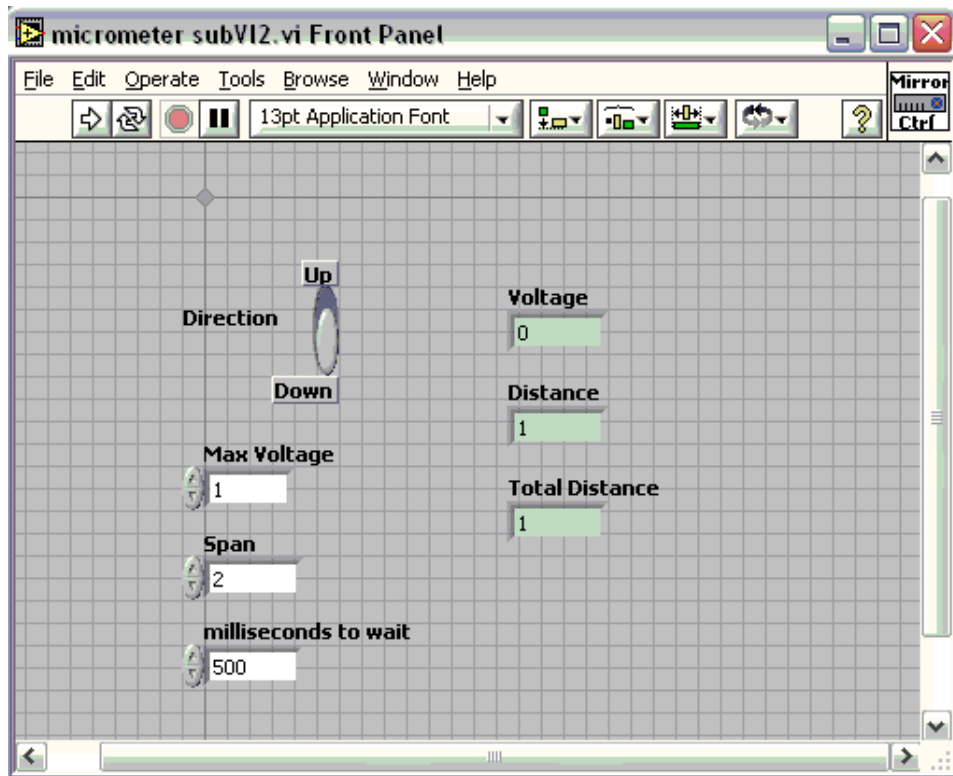


Figure B.3: Stepper motor subVI.



Figure B.4: Interface of the LCR.

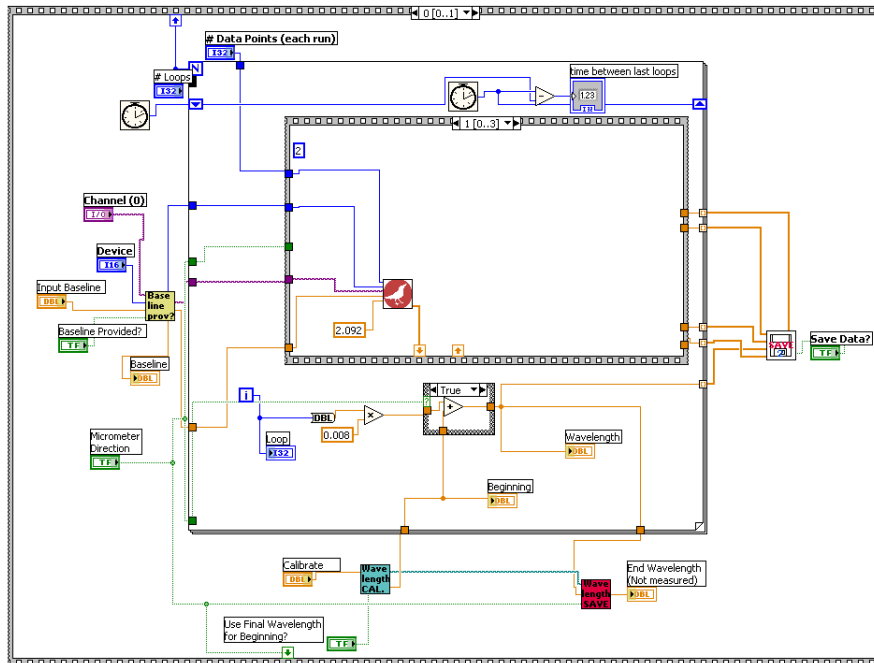


Figure B.5: Block diagram of the applied voltage on the LCR for perpendicular polarization.

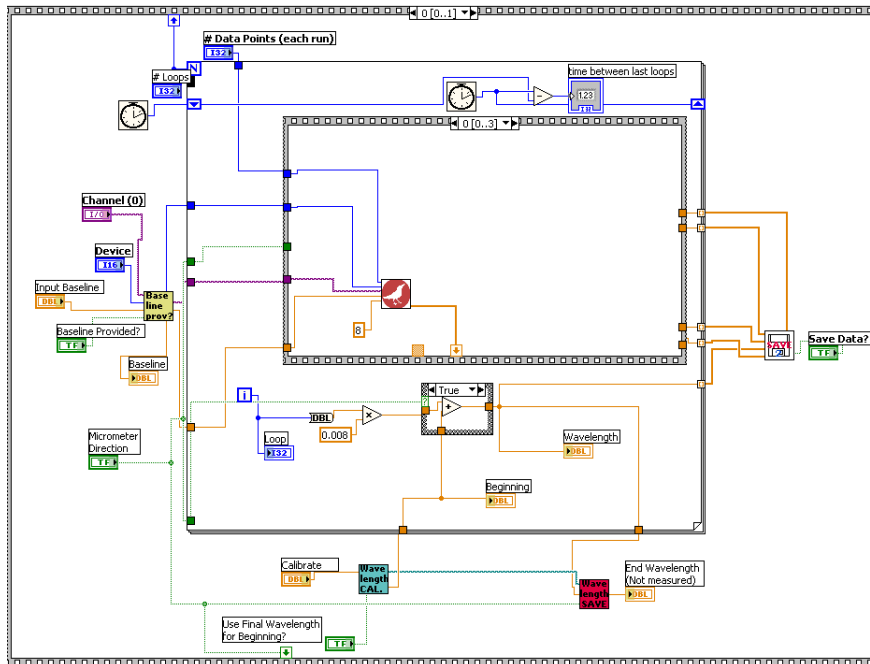


Figure B.6: Block diagram of the applied voltage on the LCR for parallel polarization.

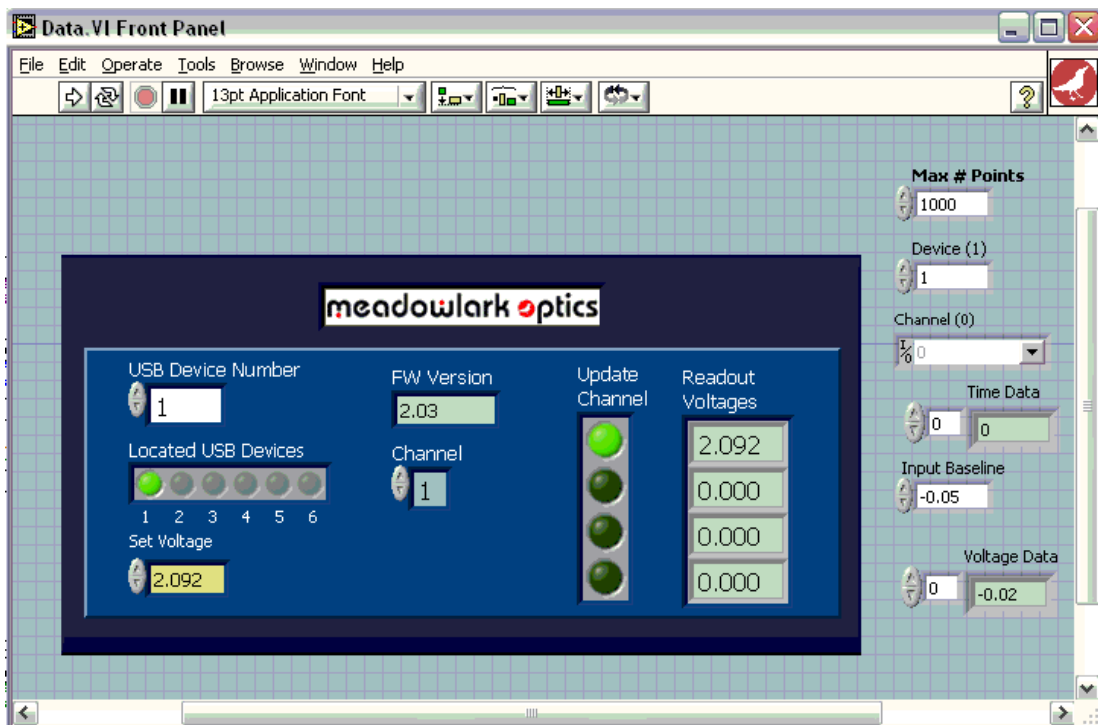


Figure B.7: Medowlark LCR subVI.

# Appendix C

## Experimental Apparatus



Figure C.1: Experimental Apparatus.

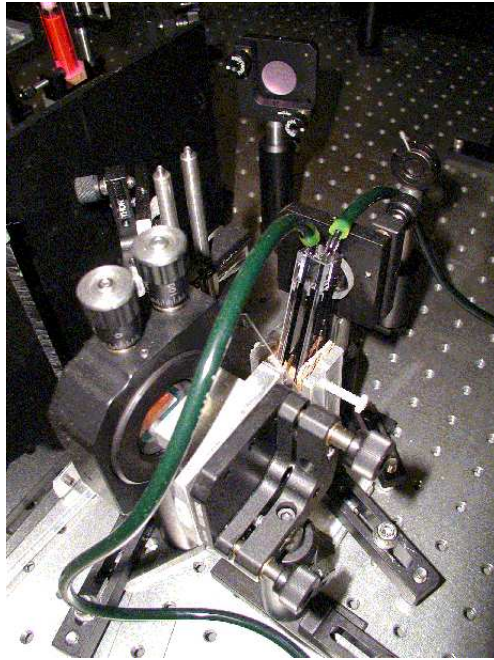


Figure C.2: Flowing dye laser 1 oscillator in the Littman-Metcalf design.



Figure C.3: Dye flowing machine for laser 1.

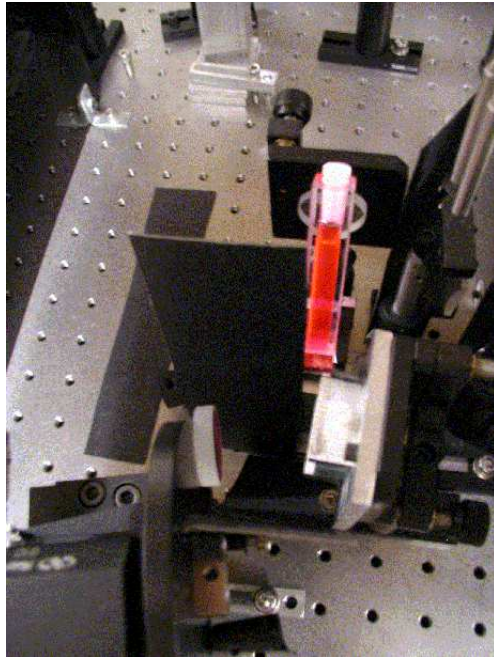


Figure C.4: Static dye laser 2 oscillator in the Littman-Metcalf design.



Figure C.5: Dye laser 2 amplifier.

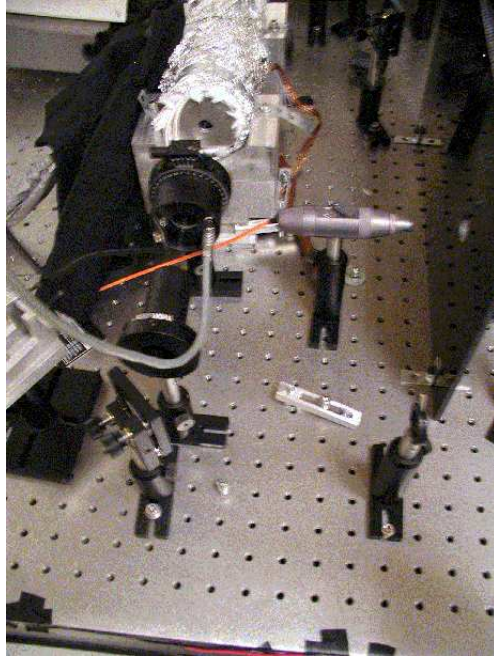


Figure C.6: A view of the LCR and Glan-Thompson polarizer.

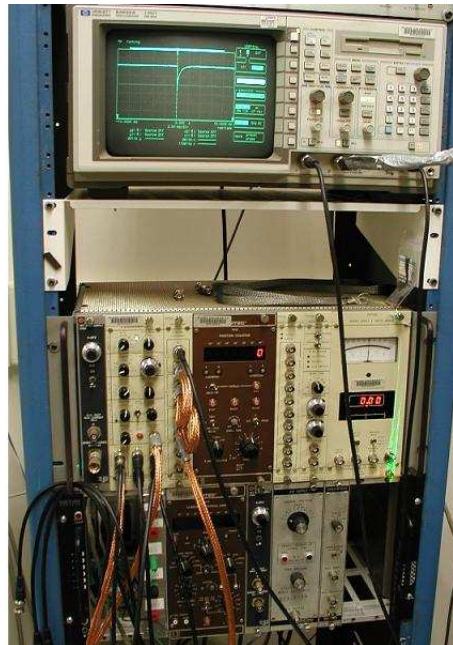


Figure C.7: Boxcar averager/integrator.

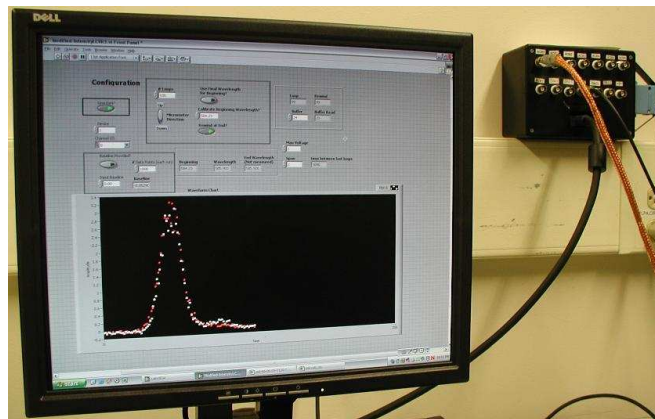


Figure C.8: DAQ board connected between a computer and the boxcar averager/integrator.